

TS23/McDonald and FIES/NOT strike again: Two new warm Jupiter systems and outer companions in a third

Downloaded from: https://research.chalmers.se, 2026-11-07 16:54 UTC

Citation for the original published paper (version of record):
Knudstrup, E., Gandolfi, D., Cochran, W. et al (2026). TS23/McDonald and FIES/NOT strike again: Two new warm Jupiter systems and outer companions in a third. Astronomy and Astrophysics, 714. http://dx.doi.org/10.1051/0004-6361/202661610

N.B. When citing this work, cite the original published paper.

research.chalmers.se offers the possibility of retrieving research publications produced at Chalmers University of Technology. It covers all kind of research output: articles, dissertations, conference papers, reports etc. since 2004. research.chalmers.se is administrated and maintained by Chalmers Library

(article starts on next page)

A&A, 714, A496 (2026)
https://doi.org/10.1051/0004-6361/202661610
© The Authors 2026

Astronomy & Astrophysics

TS23/McDonald and FIES/NOT strike again

Two new warm Jupiter systems and outer companions in a third

E. Knudstrup[1,⋆], D. Gandolfi[2], W. D. Cochran[3], M. Endl[3], P. MacQueen[3], T. Pugh[3], M. S. Lundkvist[1], C. M. Persson[4], A. Stokholm[5], M. L. Winther[1], J. R. Larsen[1], J. L. Rørsted[1], S. H. Albrecht[1], K. A. Collins[6], C. Watkins[7], B. Edwards[8,9], D. R. Ciardi[10], C. A. Clark[10], A. S. Polanski[11], C. Ziegler[12], C. Briceño[13], A. W. Mann[14], M. Everett[15], S. Howell[16], B. Safonov[17], T. Gan[18,19], K. Barkaoui[18,20,21], P. Benni[22], R. P. Schwarz[6], K. Horne[23], R. Sefako[24], and D. Muthukrishna[25,26]

(Affiliations can be found after the references)

Received 23 June 2026 / Accepted 18 September 2026

ABSTRACT

Context. Gas giant planets with orbital periods of P∼8–200 d, known as warm Jupiters, are thought to be largely unaffected by the tidal interactions that can often erase valuable information on the dynamical histories of hot Jupiters. Their orbital eccentricities (e) and stellar obliquities are therefore expected to be preserved, making them valuable probes of giant-planet formation and migration.
Aims. Our aim is to identify and characterise transiting warm Jupiters and expand the sample of well-characterised systems and enable further studies of giant-planet formation and migration.
Methods. We analysed TESS transit photometry, together with ground-based radial velocity (RV) measurements. We performed a joint fit of the photometric and spectroscopic data from the TS23 and FIES spectrographs to determine the planetary and orbital parameters.
Results. We report on the discovery and characterisation of two new, transiting warm Jupiters; TOI-5120 b ($M_p = 1.23 \pm 0.05$ M_J, $R_p = 0.969 \pm 0.017$ R_J, $P = 24.91645 \pm 0.00002$ d, $e = 0.10 \pm 0.02$) and TOI-5699 b ($M_p = 0.25 \pm 0.03$ M_J, $R_p = 0.996 \pm 0.015$ R_J, $P = 22.01850 \pm 0.00004$ d, $e = 0.30^{+0.09}_{-0.08}$). We also refined the parameters of the known warm Jupiter TOI-2158 b ($M_p = 0.87 \pm 0.04$ M_J, $R_p = 0.899 \pm 0.015$ R_J, $P = 8.60079^{+0.00002}_{-0.00001}$ d, $e = 0.028^{+0.013}_{-0.014}$). In addition, we detected an outer planetary companion, TOI-2158 c ($M_p \sin i = 1.62 \pm 0.13$ M_J, $P = 414.5^{+1.5}_{-1.6}$ d, $e = 0.54 \pm 0.04$), and identified a long-term RV trend that could indicate another planetary companion on a wide orbit.
Conclusions. The diverse architectures of these systems, particularly the presence and absence of outer companions, highlight the range of dynamical pathways leading to warm Jupiters.

Key words. planets and satellites: detection – planets and satellites: dynamical evolution and stability – planets and satellites: formation – planets and satellites: gaseous planets

1. Introduction

Hot Jupiters are giant planets on orbits characterised by a small semi-major axis ($a \lesssim 0.1$ AU), whose existence and properties have posed significant challenges to theories on planet formation theory, making them key laboratories for studying planetary migration. Warm Jupiters are found on slightly wider orbits, but still smaller than that of Earth. As for hot Jupiters, their origin remains debated and several formation and migration pathways have been proposed, including in situ formation, migration through the protoplanetary disc, and high-eccentricity tidal migration (see e.g. Dawson & Johnson 2018, for a review). Each of these mechanisms is expected to leave distinct dynamical signatures in the resulting planetary systems. In particular, the orbital eccentricity (e) and stellar obliquity (ψ) can provide clues to the dynamical history of a system, as high-eccentricity (high-e) migration can excite both quantities to large values through processes such as planet–planet scattering (e.g. Rasio & Ford 1996) or secular interactions driven by outer companions (e.g. Wu & Murray 2003); whereas disc migration, for instance, is generally believed to keep eccentricities low (e.g. Duffell & Chiang 2015).

In contrast to hot Jupiters, whose close-in orbits lead to strong tidal interactions with their host stars, warm Jupiters are expected to experience significantly weaker tidal dissipation. As a result, their orbital eccentricities and stellar obliquities may remain largely preserved over long timescales (e.g. Jackson et al. 2008; Albrecht et al. 2012). Warm Jupiter systems may therefore provide a more direct record of the processes that shaped their orbital architectures and offer a valuable window into the formation and migration of giant planets. Because tidal realignment is expected to be much less efficient for warm Jupiters than for hot Jupiters, stellar obliquities may also retain a record of their migration history. Recent obliquity measurements of warm Jupiters have so far revealed a tendency toward spin-orbit alignment, providing important constraints on their origin (e.g. Rice et al. 2022; Wang et al. 2024). Another intriguing possibility is that some warm Jupiters represent planets caught in transition, occupying an intermediate stage between cold and hot Jupiters during high-e tidal migration (e.g. Fabrycky & Tremaine 2007; Socrates et al. 2012). An often cited example is HD 80606 b, whose highly eccentric orbit suggests that it may be undergoing this process (Naef et al. 2001; Wu & Murray 2003).

Observational studies of the giant-planet population have revealed several features that might be linked to these formation

⋆ Corresponding author: emil@phys.au.dk

Open Access article, published by EDP Sciences, under the terms of the Creative Commons Attribution License (https://creativecommons.org/licenses/by/4.0), which permits unrestricted use, distribution, and reproduction in any medium, provided the original work is properly cited.
This article is published in open access under the Subscribe to Open model. Subscribe to A&A to support open access publication.

pathways. The eccentricity distribution of warm Jupiters appears to contain both low- and high-e components (e.g. Petrovich & Tremaine 2016), suggesting that multiple migration channels may contribute to the observed population. In addition, the occurrence of warm Jupiters has been connected to the presence of outer companions and to host-star metallicity (e.g. Dong et al. 2014), both of which may influence the dynamical evolution of planetary systems. These trends highlight the importance of expanding the sample of well-characterised warm Jupiter systems.

The Transiting Exoplanet Survey Satellite (TESS; Ricker et al. 2015) has significantly increased the number of known transiting giant planets (e.g. Dong et al. 2021a), providing an opportunity to discover and characterise new warm Jupiter systems. When combined with a ground-based radial velocity (RV) follow-up, TESS discoveries allow for precise measurements of planetary masses, radii, and orbital parameters to be taken, enabling detailed studies of their dynamical architectures.

In this work, we combine TESS photometry with RVs from the Tull Coudé Spectrograph (TS23: Tull et al. 1995) and the FIbre-fed Echelle Spectrograph (FIES; Frandsen & Lindberg 1999; Telting et al. 2014) to report on the discovery and characterisation of two new transiting warm Jupiters, TOI-5120 b and TOI-5699 b. Furthermore, we aim to refine the parameters of the previously discovered warm Jupiter TOI-2158 b (Knudstrup et al. 2022). We also report the detection of an outer planetary companion in the TOI-2158 system and identify a long-term radial-velocity trend, potentially caused by the presence of an additional substellar companion on a wide orbit. These systems add to the growing sample of well-characterised warm Jupiters and provide further insights into the diversity of architectures among giant-planet systems.

The paper is structured as follows. In Sect. 2, we present the various space-based and ground-based observations we used in this study. The stellar parameters derived from our spectroscopic observations are given in Sect. 3. In Sect. 4, we present our joint analysis of the photometric and spectroscopic data, along with the resulting orbital and planetary parameters. In Sect. 5, we discuss our results before drawing our conclusions in Sect. 6.

2. Observations

2.1. Photometry

The two new planet candidates, TOI-5120 and TOI-5699, were announced as TESS objects of interest (TOIs) by the TESS Science Office at MIT (Guerrero et al. 2021). This was done after transits were identified by the Massachusetts Institute of Technology (MIT) Quick Look Pipeline (QLP; Huang et al. 2020) through a box-least-squares (BLS; Kovács et al. 2002; Hartman & Bakos 2016) search of the 10-min cadence full-frame images (FFIs).

Subsequently, the targets were placed on the 2-min cadence target list. The 2-min cadence data are processed by the Science Processing Operation Center (SPOC; Jenkins et al. 2016) team at the NASA Ames Research Center, where light curves are extracted through simple aperture photometry (SAP; Twicken et al. 2010; Morris et al. 2020) and processed using the Presearch Data Conditioning (PDC; Smith et al. 2012; Stumpe et al. 2012, 2014) algorithm.

For all three systems, we downloaded and extracted the TESS observations using `lightkurve` (Lightkurve Collaboration 2018). To de-trend the light curves, we iteratively performed fits to obtain good transit parameters to temporarily remove the transits from the photometric time series. After removing the transits, we detrended the light curve using Gaussian Process (GP) regression using a Matérn-3/2 kernel from the `celerite` library (Foreman-Mackey et al. 2017). We then re-injected the transits in the time series and selected points in intervals 8 hours before and after the mid-transit times.

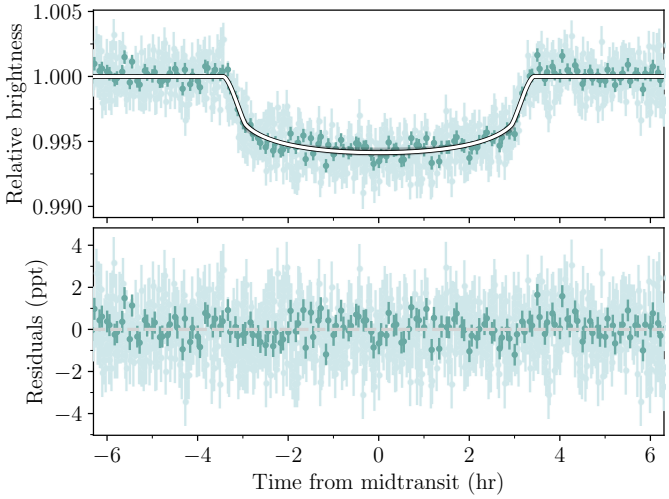


Fig. 1. TESS light curve for TOI-5120 b. The dark green markers are TESS observations taken with a cadence of 10-min and the lighter points are 2-min cadence observations. Overplotted is the best-fitting transit model for TOI-5120 b.

Ground-based time-series follow-up photometry was acquired for all three targets as part of the TESS Follow-up Observing Program (TFOP; Collins 2019) with the aim of: (i) ruling out or identifying nearby eclipsing binaries; (ii) identifying transit-like events for the target to verify their depth, thereby determining the TESS photometric deblending factor; (iii) refining the ephemeris; and (iv) imposing constraints on variations in transit depth across different optical filter bands. Transit observations were scheduled using the `TESS Transit Finder`, a customized version of the `Tapir` software package (Jensen 2013). For the ground-based observations, image calibration and photometric data extraction were performed using the `AstroImageJ` software package (Collins et al. 2017).

We observed TOI-5120 with the CHaracterising ExOPlanet Satellite (CHEOPS; Benz et al. 2021) on two separate dates as part of programme AO3-34 with the aim of refining the TESS ephemerides for targets that are potentially well-suited for atmospheric follow-up with the Atmospheric Remote-sensing Infrared Exoplanet Large-survey (Ariel; Tinetti et al. 2018) mission. The CHEOPS light curves were detrended using the `PYCHEOPS` package (Maxted et al. 2022).

All the photometric observations for TOI-5120, TOI-5699, and TOI-2158 are shown in Figs. B.11, B.12, and B.13, respectively. The space- and ground-based photometric observations are summarised in Tables A.1 and A.5, respectively.

2.1.1. TOI-5120

TOI-5120 was observed with a cadence of 10-min in TESS Sectors 44 and 45. The system was observed again in Sectors 71 and 72, this time in 2-min cadence. The TESS light curves centred around mid-transit for TOI-5120 b is shown in Fig. 1. The system was also observed in Sector 1751 (special pointing to observe the interstellar comet 3I/ATLAS), but the seven days of observations did not include a transit.

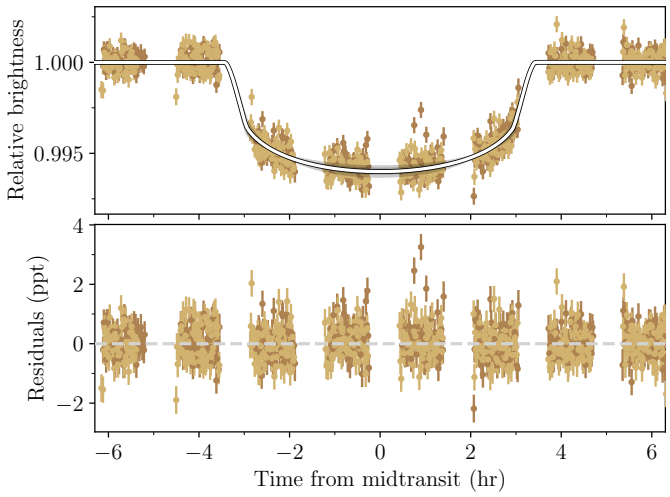


Fig. 2. CHEOPS light curve for TOI-5120 b. The brown points are the CHEOPS observations from December 2022, while tan are observations from February 2024. As in Fig. 1 the best-fitting transit model is overplotted.

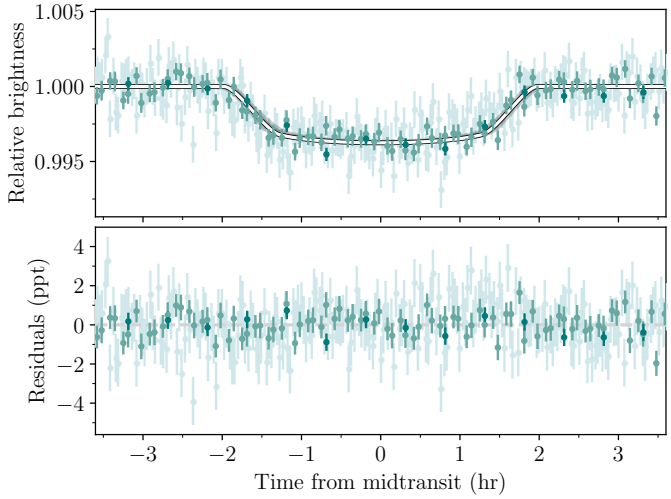


Fig. 3. TESS light curve for TOI-5699 b. Going from the darkest to the lightest colors the markers show the 30-min, 10-min, and 2-min TESS observations. The best-fitting transit model for TOI-5699 b is overplotted.

Two transits of TOI-5120 b were observed with CHEOPS; observations were carried out from (UTC) 02:49 to 20:07 on 2022-12-30 and from 17:50 on 2024-02-01 to 13:09 on 2024-02-02. The observations were taken with a cadence of 1 min, but with the characteristic gaps from the sun-synchronous orbit of the spacecraft. The CHEOPS observations are shown in Fig. 2.

Ground-based photometric transit observations were made on four separate nights with four different filters (i', r', B, z-short), No full transits were observed, but the observations covered either ingress or egress plus a sizable segment (> 50%) of the transit. The ground-based observations are shown in Fig. B.6.

2.1.2. TOI-5699

TOI-5699 was observed by TESS in Sector 25 with 30-min cadence and in Sectors 51 and 52 at a 10-min cadence. In Sectors 78 and 79, TOI-5699 was observed with a cadence of 2 min, but given the long orbital period ($P \sim 25$ d) no transit occurred during the Sector 78 observations. The phase-folded TESS light curves of TOI-5699 b are shown in Fig. 3.

A full transit of TOI-5699 b was observed from ground in the z-short filter. This transit is shown in Fig. B.7.

2.1.3. TOI-2158

Two sectors from TESS were included in Knudstrup et al. (2022), namely: Sector 26 (30-min cadence) and Sector 40 (2-min cadence). TOI-2158 has since been observed by TESS in Sector 53, also with a cadence of 2 min.

In addition to the TESS photometry, we included the ground-based photometry from the Las Cumbres Observatory Global Telescope (LOCGT; Brown et al. 2013) presented in Knudstrup et al. (2022), where three complete transits were observed (separately) in the i', B, and z-short filters. The TESS and ground-based observations centred around the mid-transit time are displayed in Figs. 4 and B.8, respectively.

2.2. RV follow-up

Our RV monitoring was carried out using the TS23 spectrograph mounted at the 2.7 m Harlan J. Smith telescope at the

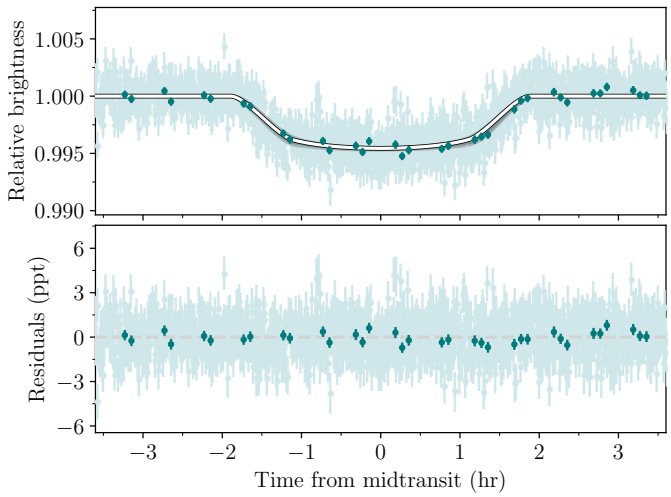


Fig. 4. TESS light curve for TOI-2158 b. The darker green markers are TESS observations taken with a cadence of 30-min and the lighter points are 2-min cadence observations. Overplotted is the best-fitting transit model for TOI-2158 b.

McDonald Observatory, Texas, USA, and the FIES spectrograph at the 2.6 m Nordic Optical Telescope (NOT; Djupvik & Andersen 2010) of the Roque de los Muchachos observatory, La Palma, Spain.

For the TS23 observations an I_2 gas cell was placed in the light beam to allow for the extraction of high precision RVs. All spectra were reduced and extracted through standard IRAF tasks, and RVs were extracted by making use of the Austral code (Endl et al. 2000). TS23 Observations of each target were divided into three separate successive exposures to enable removal of energetic particle hits on the detector using the IRAF `crcombine` routine.

FIES spectra were reduced following the procedure outlined in Gandolfi et al. (2015). This includes bias subtraction, flat fielding, order tracing, and extraction as well as wavelength calibration. As with the TS23 exposures, science exposures were

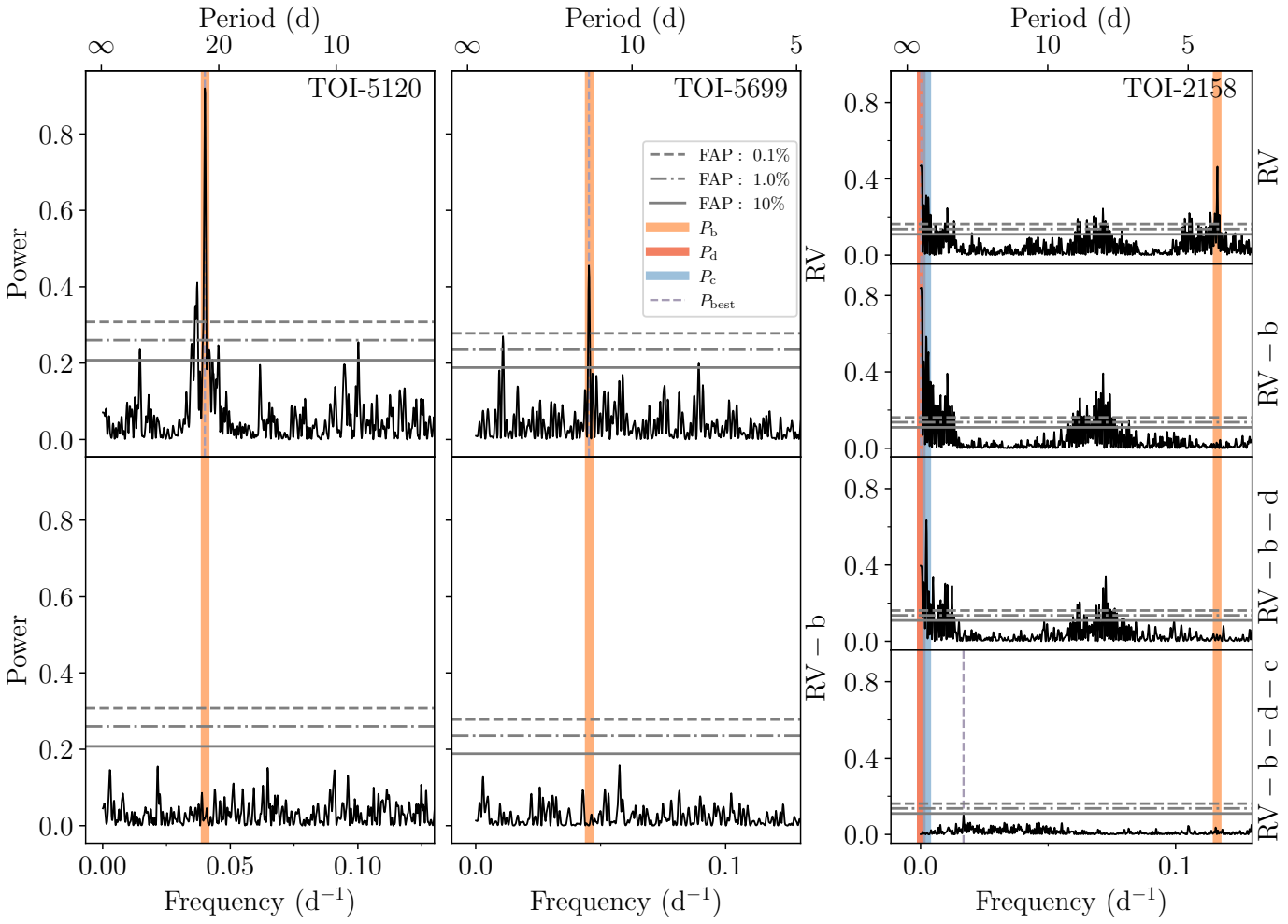


Fig. 5. Lomb-Scargle periodogram created from our RVs. The first two columns display the periodograms for the RVs obtained for TOI-5120 (*left*) and TOI-5699 (*middle*) with the raw RVs shown on top and after subtracting the best-fitting Keplerian orbit on the bottom (see Sect. 4). In the rightmost column we show the RVs for TOI-2158 again with the raw RVs on top and then subtracting the best-fitting Keplerian from planet b, then from planet (or signal) d in the panel below, and lastly planet c in the panel at the bottom. The period of planet b is denoted with an orange line and planet c and d (TOI-2158) in blue and red, respectively. The frequency of the highest peak in the periodogram is shown as the dashed line. We also give the FAPs at 0.1%, 1.0%, and 10%.

divided into three sub-exposures (i.e. an exposure of 2700 s consisted of three exposures of 900 s) to mitigate the effects of energetic particles, and we performed a sigma clipping algorithm when combining the frames. To trace the instrumental RV drift, we acquired long-exposed thorium-argon (ThAr) spectra immediately before and after each block of science exposures. Finally, the RVs were extracted from multi-order cross-correlations, where the first stellar spectrum was used as a template. All RVs are tabulated in Table A.2.

We monitored TOI-5120 with both TS23 and FIES starting 2022-02-10, and continuing until 2025-12-17, meaning a baseline of 1406 d. We collected a total of 56 RVs using TS23 and 20 RVs using FIES, which are shown in Fig. B.11. We monitored TOI-5699 with TS23 between February 2023 and March 2026, collecting 86 RVs. Three epochs were discarded due to dome vignetting. We furthermore collected four RVs using FIES starting observations in May and ending in June 2025. The baseline is thus 1128 d. The RV time series is shown in Fig. B.12.

As mentioned, our RV follow-up for TOI-2158 presented here is a continuation of the efforts from Knudstrup et al. (2022). In addition to the 8 d signal from the orbital period of TOI-2158 b a long-term quadratic trend was seen in the RVs. We therefore continued to monitor the system with both TS23 and FIES. The RV monitoring in Knudstrup et al. (2022) was carried out from 2021-03-03, to 2022-06-03, with 33 RVs from TS23 and 38 from FIES. Here we have extended the monitoring until 2026-01-26, resulting in a total of 112 TS23 RVs and 53 FIES RVs with a baseline of 1764 d. As mentioned in Knudstrup et al. (2022), the FIES spectrograph was refurbished on 2021-07-01, which has introduced an RV offset between observations taken before and after this date. We have therefore treated our FIES observations as coming from two separate spectrographs; FIES (before) and FIES+ (after). All RVs for TOI-2158 are displayed in Fig. B.13.

In Fig. 5, we show the Lomb-Scargle periodograms (VanderPlas et al. 2012; VanderPlas & Ivezić 2015) created from the RVs we have collected for all three systems. We also highlight the period of the transiting planet in orange and as indicated by the false alarm probabilities (FAPs), the transiting planets are clearly detected in all three systems. For TOI-2158 we also see additional peaks; one at around 5400 d and one at 440 d. The former of the two is not resolved as our baseline for TOI-2158 is only 1625 d and is therefore only seen as a long-term trend, potentially coming from a rather massive companion on a wide orbit. For the latter we have covered roughly

four cycles and we interpret this as an additional planet in the system.

2.3. High-resolution imaging

As part of the standard process for validating transiting exoplanets to assess the possible contamination of bound or unbound companions on the derived planetary radii (Ciardi et al. 2015), we observed TOI 5120 with optical speckle observations and TOI-5699 with optical speckle and near-infrared (NIR) adaptive optics (AO) imaging. A faint ($\Delta I \approx 5.5$ mag) and potentially bound companion was detected in the TOI-5120 system. Below we summarise the high-resolution imaging observations.

2.3.1. Optical speckle imaging

We searched for stellar companions to TOI-5120 with speckle imaging on the 4.1-m Southern Astrophysical Research (SOAR) telescope (Tokovinin 2018) on 2022-04-15, observing in the Cousins I band, a similar visible band-pass as TESS. This observation was sensitive to a 5.2-magnitude fainter star at an angular distance of 1″ from the target. More details of the observations within the SOAR TESS survey are available in Ziegler et al. (2020). The 5σ detection sensitivity and speckle auto-correlation functions from the observations are shown in Fig. B.1. No nearby stars were detected within 3″of TOI-5120 in the SOAR observations.

NESSI (NN-EXPLORE Exoplanet and Stellar Speckle Imager; Scott et al. 2018) is a speckle imager installed at the WIYN 3.5 m telescope on Kitt Peak. NESSI normally collects simultaneous speckle images in two filters, but for the night of 2022-04-18 when TOI-5120 was observed, only one beam was operational. NESSI data are therefore only available in one filter at $\lambda_c = 832$ nm. The observation consisted of a set of 9000 speckle frames of 40 ms each. The field-of-view was confined using a readout region of 256 × 256 pixels or 4.6 × 4.6″. Additional observations of a single star near TOI-5120 were obtained for calibration of the underlying PSF.

To reduce the data, we used the pipeline described by Howell et al. (2011). Speckle data are best used to constrain the presence of additional sources out to a radius of ∼1.2″ from the target star, but sources may be measured at greater radii with slightly reduced photometric accuracy. Pipeline data products include a reconstructed image of the field around each target and, measured from that, a contrast curve representing the relative magnitude limit as a function of angular separation from the star. There was a single, fainter companion star detected close to TOI-5120. The companion lies at an angular separation of 1.298″ and a position angle (PA), as measured from North through East, of 152.74° (corresponding to a physical separation of ∼300 AU). The magnitude contrast with TOI-5120 is 5.51 magnitudes in the 832 nm filter.

TOI-5120 and TOI-5699 were observed on 2022-12-24 and 2023-01-01, respectively, with the speckle polarimeter on the 2.5-m telescope at the Caucasian Observatory of Sternberg Astronomical Institute (SAI) of Lomonosov Moscow State University. A low-noise CMOS detector was used for the observations (Strakhov et al. 2023). The atmospheric dispersion compensator was active, which made it possible to use the I_c band. The respective angular resolution is 0.083″. The resulting sensitivity curves and autocorrelation functions (ACFs) are shown in Figs. B.2 and B.5 for TOI-5120 and TOI-5699, respectively.

For TOI-5120 we once again detected a stellar companion at a separation of 1.26 ± 0.01″, position angle 153.3 ± 0.4°, and the magnitude difference is $\Delta I_c = 5.7 \pm 0.1$. We reobserved TOI-5120 on 2024-10-13. The companion was confirmed at a separation of 1.29 ± 0.01″, PA of 152.6 ± 0.3°, and ΔI_c = 6.0 ± 0.1. The detections from the three epochs are summarised in Table 1. The position of the component did not change significantly while from proper motion a change of 118.7 mas is expected on a time base of 1.8 yr for a background star. The component is likely to be physically bound. We note that the component is missing in the *Gaia* DR3 catalogue despite the large separation, although given the large brightness contrast the companion could go undetected at this separation (El-Badry et al. 2021). Furthermore, the *Gaia* renormalised unit weight error (RUWE) is 1.034, indicating a clean single-source astrometric solution with no evidence that the companion measurably perturbed the astrometry. No other companions were detected. The detection limits at distances 0.25 and 1.0″ from the star are $\Delta I_c = 3.8^m$ and 6.5^m for TOI-5120 and $\Delta I_c = 3.8^m$ and 5.6^m for TOI-5699.

Table 1. Speckle observations of TOI-5120.

Date (UTC)	Separation (″)	PA (°)	Δm (832 nm/I_c)
2022-04-18	1.298	152.74	5.51
2022-12-24	1.26 ± 0.01	153.3 ± 0.4	5.7 ± 0.1
2024-10-13	1.29 ± 0.01	152.6 ± 0.3	6.0 ± 0.1

Notes. Separation, position angle (measured from north to east), and contrast of the companion in TOI-5120, which we note is not detected in *Gaia* DR3. The first observation is from NESSSI and the two others are from SAI.

TOI-5699 was observed on 2024-05-22 at Gemini North 8-m telescope using the 'Alopeke speckle imager. The star has no close companions to within the angular (0.02–1.2″) and 5σ magnitude contrast levels (5–8.5 mags) determined in each of two filters. The 5σ contrast curves and the 832 nm reconstructed image are shown in Fig. B.3. No companion was detected.

For good measure, we further note that speckle polarimetry for TOI-2158 has also been obtained. No companions were detected in this system from these observations. Details and plots can be found in Knudstrup et al. (2022).

2.3.2. NIR AO imaging

Observations of TOI 5699 were made on 2023-06-07 with the PHARO instrument (Hayward et al. 2001) on the Palomar Hale (5m) telescope behind the P3K natural guide star AO system (Dekany et al. 2013) in the narrow-band Br-gamma filter (λ_o = 2.29; $\Delta\lambda$ = 0.035 μm). The PHARO pixel scale is 0.025″ per pixel. A standard 5-point quincunx dither pattern with steps of 5″was performed three times with each repeat separated by 0.5″. The reduced science frames were combined into a single mosaicked image with a final resolution of 0.1″. The sensitivity of the final combined AO image were determined by injecting simulated sources azimuthally around the primary target every 20° at separations of integer multiples of the central source's full width at half maximum (FWHM; Furlan et al. 2017). The brightness of each injected source was scaled until standard aperture photometry detected it with 5σ significance. The final 5σ limit at each separation was determined from the average of all of the determined limits at that separation, and the uncertainty on the limit was set by the root-mean-square (rms) dispersion of the azimuthal slices at a given radial distance. The Palomar imaging and sensitivities are shown in Fig. B.4. The IR imaging

Table 2. Stellar parameters.

	TESS object of interest TESS input catalogue TYCHO-2	TOI-5120 TIC 58723861 TYC 1894-00102-1	TOI-5699 TIC 224328450 TYC 2582-02794-1	TOI-2158 TIC 342642208 TYC 1577-691-1
V [a]	Tycho V magnitude	10.792 ± 0.011	10.860 ± 0.007	10.887 ± 0.006
B [a]	Tycho B *Gaia*	11.6 ± 0.2	11.55 ± 0.10	11.66 ± 0.09
T [b]	TESS magnitude	10.233 ± 0.006	10.449 ± 0.006	10.167 ± 0.006
G [c]	*Gaia* G magnitude	10.667 ± 0.003	10.857 ± 0.003	10.673 ± 0.003
$G_{\rm BP}$ [c]	*Gaia* $G_{\rm BP}$ magnitude	10.992 ± 0.003	11.156 ± 0.003	11.071 ± 0.003
$G_{\rm RP}$ [c]	*Gaia* $G_{\rm RP}$ magnitude	10.175 ± 0.004	10.391 ± 0.004	10.108 ± 0.004
$\alpha_{\rm J2000}$ [c]	Right ascension	06:56:51.371	16:44:54.288	18:27:14.461
$\delta_{\rm J2000}$ [c]	Declination	+22:35:44.627	+31:12:39.317	+20:31:36.671
μ_α [c]	Proper motion in RA (mas yr^{-1})	6.13 ± 0.07	−8.69 ± 0.04	−44.00 ± 0.04
μ_δ [c]	Proper motion in Dec (mas yr^{-1})	−65.60 ± 0.06	−35.20 ± 0.05	7.89 ± 0.07
ϖ [c]	Parallax (mas)	4.496 ± 0.016	3.303 ± 0.011	5.116 ± 0.013
π [c]	Distance (pc)	230 ± 2	305 ± 2	198.5 ± 1.4
γ [c]	Systemic velocity (km s^{-1})	16.33 ± 0.53	6.06 ± 0.26	−108.55 ± 0.17
RUWE [c]	Renormalised unit weight error	1.034	0.871	1.003
$T_{\rm eff}$ [d]	Effective temperature (K)	5763 ± 90	5905 ± 100	5673 ± 50
$\log g_\star$ [d]	Surface gravity (cgs)	4.18 ± 0.07	4.05 ± 0.07	4.19 ± 0.05
[Fe/H] [d]	Metallicity (dex)	0.2 ± 0.07	0.11 ± 0.05	0.47 ± 0.08
$v \sin i_\star$ [d]	Projected rotational velocity (km s^{-1})	4.8 ± 0.9	4.3 ± 1.2	3.7 ± 0.5
$\xi_\star$ [e]	Micro-turbulent velocity (km s^{-1})	1.04	1.12	1
$\zeta_\star$ [f]	Macro-turbulent velocity (km s^{-1})	3.7	4.34	3.49
$R_\star$ [g]	Radius ($R_\odot$)	1.42 ± 0.05	1.64 ± 0.06	1.32 ± 0.04
$M_\star$ [g]	Mass ($M_\odot$)	1.12 ± 0.05	1.13 ± 0.04	1.12 ± 0.05
$\rho_\star$ [g]	Density (g cm^{-3})	0.55 ± 0.07	0.36 ± 0.04	0.69 ± 0.06
τ [g]	Age (Gyr)	7.5 ± 1.5	6.6 ± 0.7	7.7 ± 1.6

Notes. [a] Tycho-2 (Høg et al. 2000). [b] TICv8.2 (Stassun et al. 2019). [c] *Gaia* DR3. [d] This work using SME, except for TOI-2158 where the parameters are from Knudstrup et al. (2022). [e] Empirical relation (Bruntt et al. 2010). [f] Empirical relation (Doyle et al. 2014). [g] This work using BASTA.

detected no stellar companions, in agreement with the speckle observations.

3. Stellar parameters

To derive the stellar parameters for the three host stars, we used our high-resolution spectroscopic observations for each target. This was done by co-adding our FIES observations to create a high signal-to-noise (S/N) spectrum.

3.1. Spectral analysis

In the spectral analysis we used the empirical code `SpecMatc-Emp` (Yee et al. 2017) to obtain initial values for the subsequent spectral modelling. The primary quantities of interest in our spectral analysis are the effective temperature ($T_{\rm eff}$), the surface gravity ($\log g$), and the metallicity ([Fe/H]).

Following the approach in Persson et al. (2018), we made use of Spectroscopy Made Easy (SME; Valenti & Piskunov 1996; Piskunov & Valenti 2017) for the more detailed analysis. SME fits observations to synthetic computed spectra, where we opted to use the MARCS grid of stellar atmospheres (Gustafsson et al. 2008) with retrieved atomic and molecular line data from the Vienna Atomic Line Database (VALD; Ryabchikova et al. 2015). In our analysis we varied one parameter at a time. We started out by estimating $T_{\rm eff}$ from the line wings of the H_α line after which we determined [Fe/H], [Ca/H], and [Na/H] from clean and unblended lines between 6000 and 6500 Å. We then used the line wings of the Ca lines at 6102 Å, 6122 Å, 6162 Å, as well as the Ca line at 6439 Å to determine $\log g$. We then iterated this process until the values had converged. Micro- ($\xi_\star$) and macroturbulence ($\zeta_\star$) were estimated at each step from the resulting stellar parameters using the empirical relations from Bruntt et al. (2010) and Doyle et al. (2014), respectively. The resulting parameters are given in Table 2.

In Table A.6, we compare our spectroscopic values for all three systems with those from *Gaia* Data Release 3 (Gaia Collaboration 2023) and the Exoplanet Follow-up Observation Program (ExoFOP) website. We generally find good agreement between these parameters. We furthermore list the calcium and sodium abundances there.

3.2. Stellar properties

To determine the stellar properties, we used the BAyesian STellar Algorithm (BASTA; Silva Aguirre et al. 2015; Aguirre Børsen-Koch et al. 2022). This is a Bayesian framework which computes the posterior distributions of each stellar property such as stellar mass, radius, and age given a set of observations and potentially a set of priors. For observational constraints, we choose to use our spectroscopic values ($T_{\rm eff}$, $\log g$, [Fe/H] as derived with SME for TOI-5120 and TOI-5699, and as reported in Knudstrup et al. 2022 for TOI-2158; see below), along with

the *Gaia* apparent magnitudes and parallax (see Table 2). We corrected our parallaxes for the known parallax zero-point correction following Lindegren et al. (2021). When fitting with BASTA, we used a custom grid computed with the Garching Stellar Evolution Code (GARSTEC; Weiss & Schlattl 2008), using the same input physics as described in Winther et al. (2023) and Larsen et al. (2025), with the grid parameter ranges listed in Table A.3. For all three stars we got consistent results when using BaSTI isochrones (Hidalgo et al. 2018, opting for the models including convective core overshooting, microscopic diffusion, and mass loss) instead of the custom grid. As an additional check, we also made use of the ARIADNE[1] (Vines & Jenkins 2022) package to perform an analysis of the broad-band spectral energy distribution (SED) of the star to derive an empirical measurement of the stellar radius. The resulting parameters are listed in Table A.7 in excellent agreement with those found using BASTA.

The initial modelling results of TOI-2158 (using the values from SME in Table A.6) showed a stellar age consistent with 13.7 Gyr. While this is physically permitted by the physics governing stellar evolution, it is difficult to reconcile with the star's chemical composition in the broader context of Galactic evolution. The chemical composition of the star is notably complex, exhibiting supersolar abundances of iron, calcium, and sodium. Since the composition of a star broadly reflects that of the natal gas cloud from which it formed, Galactic chemical evolution models predict that stars born during the earliest epochs of the Milky Way should generally be metal-poor and deficient in these elements. This is because the nucleosynthetic channels responsible for enriching the interstellar medium in Fe, Ca, and Na require multiple generations of stellar evolution and supernova feedback before supersolar abundances can be reached. Consequently, within the current understanding of the Milky Way's chemical enrichment history (Matteucci 2021; Spitoni et al. 2023), it is highly implausible that a star with such enhanced abundances could have formed as early as 13.7 Gyr ago.

Spectroscopic analysis of metal-rich stars is notoriously challenging due to the many degeneracies inherent in spectral fitting (e.g. Blanco-Cuaresma et al. 2014; Slumstrup et al. 2019). Metal-rich spectra contain a large number of absorption lines, making it considerably more difficult to robustly determine the chemical composition compared to spectra of somewhat lower metallicity (e.g. Gray 2005; Jofré et al. 2019). This ambiguity has direct consequences for the age inference: a higher metallicity implies more bound-bound and bound-free transitions within the stellar interior, increasing the opacity and suppressing the outward energy flux. A high-metallicity star is therefore intrinsically fainter than a lower-metallicity counterpart of the same mass and age, and to reproduce the observed luminosity, the best-fit stellar model must invoke a more evolved and consequently older star.

As a consistency check, we computed the Galactic orbit of all three stars using the astrometric information and line-of-sight velocity from *Gaia* DR3 (Gaia Collaboration 2023). We computed the Galactic orbital properties using `galpy` (Bovy 2015), adopting the axisymmetric gravitational potential from McMillan (2017) as a model for the Milky Way. For the solar position and velocity, we assumed $(X_\odot, Y_\odot, Z_\odot) = (8.2, 0, 0.0208)$ kpc, with a circular velocity of $240\,\mathrm{km\,s^{-1}}$ (Schönrich et al. 2010; Bovy 2015; Bennett & Bovy 2019; GRAVITY Collaboration 2019). The orbits of all three stars are consistent with those of the Sun and other members of the Galactic disk as shown in Figs. B.9 and B.10. This kind of orbit is more typical of a younger, dynamically settled population than of a relic from the earliest epochs of the Milky Way, when the merger history of the Galaxy would have produced far more chaotic orbital configurations.

We therefore opted to use the spectroscopic parameters from Knudstrup et al. (2022) derived from spectra from the Tillinghast Reflector Echelle Spectrograph (TRES; Fűrész 2008) using the stellar parameter classification (SPC; Buchhave et al. 2012) tool. Adopting this earlier solution as input to BASTA infers a significantly younger age of 7.7 ± 1.6 Gyr, which is more consistent with our expectation from Galactic chemical enrichment models and with the derived Galacitic orbit. The results for all three systems are given in Table 2.

4. Joint analysis

The transit and orbital parameters were estimated through a joint modelling of the transit photometry and RVs, where we sampled the posterior distributions through a Markov chain Monte Carlo (MCMC) sampling, utilizing the `emcee` package (Foreman-Mackey et al. 2013).

The light curves were modelled using the `batman` package (Kreidberg 2015) based on the formalism from Mandel & Agol (2002). For the photometric time series acquired with cadences of 10 min or more, we created evenly spaced model light curves over which we integrated to mimic a cadence of 2 min. We modelled the stellar limb darkening using a standard quadratic law. The coefficients were obtained from the tables by Claret et al. (2013) and Claret (2018) using values appropriate for $T_{\rm eff}$, $\log g$, and [Fe/H] for each star (Table 2). During the MCMC sampling we were stepping in the sum of the coefficients applying a gaussian prior with a width of 0.1, while keeping the difference fixed at the initial value. The limb darkening coefficients can be found in Table A.4.

The RVs were modelled as Keplerian orbits, where the systemic velocities (γ) were included for each instrument. Likewise, a jitter term (ς) was added in quadrature to the RV errors stemming from a given instrument. When fitting the eccentricity, we used the $h = \sqrt{e}\cos\omega$ and $k = \sqrt{e}\sin\omega$ parametrisation, instead of stepping in e and ω (argument of periastron). For each system we also carried out runs assuming circular ($e = 0$) orbits, and below we discuss the preferred solution.

Our likelihood is defined as

$$\ln\mathcal{L} = -0.5\sum_{i=1}^{N}\left[\frac{(O_i - C_i)^2}{\sigma_i^2} + \ln 2\pi\sigma_i^2\right] + \sum_{j=1}^{M}\ln\mathcal{P}_j, \quad (1)$$

where N denotes the total number of data points (photometric and RVs); C_i the calculated model corresponding to the observed datum O_i with associated uncertainty σ_i. $\mathcal{P}_j$ is the prior applied to the jth parameter, for which we use a uniform prior unless explicitly stated otherwise.

We initialised our MCMC in a 'tight Gaussian ball' around the best-fitting solution (obtained from a least-squares fit). We assessed the convergence through visual inspection of the chains and correlation plots as well as by computing the ratio between the length of the chains to the autocorrelation time. Here we demanded that the minimum ratio was more than 100.

4.1. TOI-5120

As pointed out by Lucy & Sweeney (1971), the positive-definite nature of the orbital eccentricity introduces a bias for eccentric

[1] https://github.com/jvines/astroARIADNE/tree/master

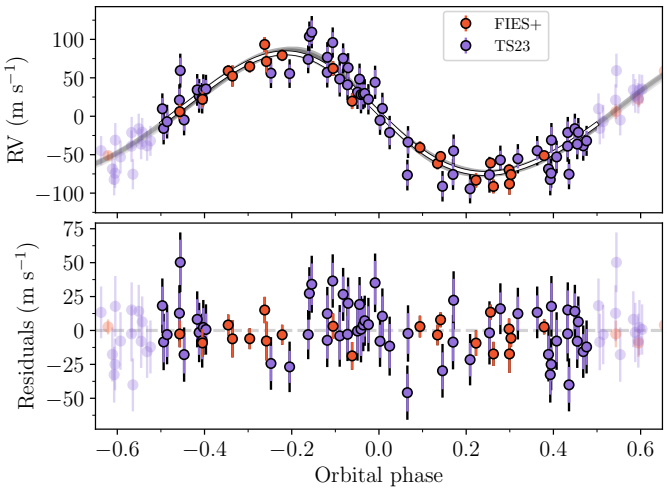


Fig. 6. RV curve for TOI-5120 b. RVs from TS23 are shown with purple markers and FIES+ RVs are shown with orange. The best-fitting RV curve is overplotted. The grey shaded regions show the 1 and 2σ confidence intervals. Low opacity markers are repeated data points shifted by one orbital phase.

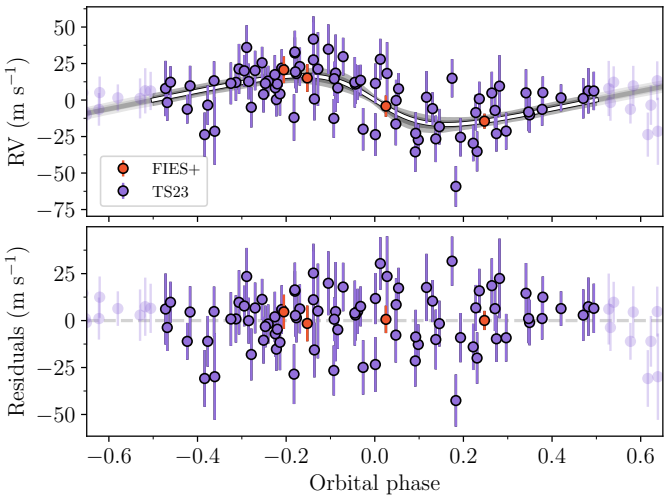


Fig. 7. RV curve for TOI-5699 b. RVs from TS23 are shown with purple markers and FIES+ RVs with orange markers. The best-fitting RV curve is overplotted. The grey shaded regions show the 1 and 2σ confidence intervals.

solutions and to be 95% confident that an eccentricity is non-zero, the result must be above 2.45σ. Allowing e to vary in TOI-5120 resulted in an eccentricity of 0.10 ± 0.02 – a modest, but significant value.

To assess which model is preferred we calculated the Bayesian Information Criterion (BIC) from both of these runs. The difference in BIC (ΔBIC) came out to be ΔBIC = 12.96 in favour of the eccentric model, which is our preferred model. The best-fitting space-based light curves are shown in Figs. 1 and 2, and in Fig. B.6 we show the ground-based light curves. The best-fitting (eccentric) RV model is displayed in Fig. 6. The best-fitting parameters are summarised in Table 4, and in Table A.8 we list the best-fitting parameters for the $e = 0$ case. Posterior distributions of key stepping parameters for TOI-5120 can be found in Fig. B.14.

4.2. TOI-5699

As for TOI-5120 we investigated both a circular and an eccentric orbit for TOI-5699. When leaving $h = \sqrt{e}\cos\omega$ and $k = \sqrt{e}\sin\omega$ free to vary, we find an eccentricity of $0.30^{+0.09}_{-0.08}$, a little over a 3σ significance. However, calculating the BIC for both scenarios yields a ΔBIC = 3.20 slightly in favour of the circular model. We also calculated the Akaike Information Criterion (AIC), with a ΔAIC = −494.57 in favour of the eccentric solution, signifying that the likelihood is greatly improved for an eccentric orbit, although the inclusion of two extra parameters are not justified according to the ΔBIC.

To further assess the significance of the orbital eccentricity and whether it is data-driven or instead a consequence of the $e \geq 0$ boundary, we performed an additional eccentric fit in which a prior was applied to the eccentricity. We adopted a Gamma prior, $\Gamma(\alpha, \beta)$, using the values $\alpha = 1.30$ and $\beta = 5.88$ from Stevenson et al. (2025). As this distribution is designed to counteract the positive-definite bias of eccentricity near $e = 0$, the inferred eccentricity would be expected to collapse toward zero if it were purely a boundary effect. The resulting posterior yielded $e = 0.26 \pm 0.09$, indicating that the eccentricity survives a skeptical prior. Applying the commonly used Beta prior from Kipping (2013, $B(0.867, 3.03)$) instead yielded $e = 0.27^{+0.11}_{-0.08}$.

We performed 5000 bootstrap realisations and computed the fraction of trials in which the fitted eccentricity was greater than or equal to the best-fitting value measured from the original data ($e \geq 0.32$). We find that this occurs in approximately 10% of the realizations, indicating that an eccentricity of this magnitude can arise from noise alone with non-negligible probability under the assumption of a circular orbit. Thus, the bootstrap test provides only weak evidence for a non-zero eccentricity, and the RV data alone are insufficient to confidently reject a circular solution.

Finally, we tested what constraints on e one can obtain from the photoeccentric effect (Seager & Mallén-Ornelas 2003). We performed an MCMC analysis of the transit photometry, imposing a prior on the stellar density ($\rho_\star = 0.36 \pm 0.04$ g cm^{-3}) derived (independently) from our stellar characterization. The RV data were excluded from this fit. This yielded an eccentricity of $e = 0.16^{+0.08}_{-0.16}$.

We therefore conclude that the data favour a mildly eccentric orbit, but the evidence is not strong enough to unambiguously rule out a circular solution. We further note that the tidal circularisation timescale is of the order of 140 Gyr (calculated using Eq. (2) in Adams & Laughlin 2006, assuming a tidal quality factor of $Q_\mathrm{p} = 10^6$), meaning that an eccentric orbit is at least physically allowed. We show the best-fitting model for the TESS light curve in Fig. 3 and the best-fitting eccentric RV model in Fig. 7. Posteriors from the eccentric run are summarised in Table 4 and for the $e = 0$ case in Table A.8. The ground-based light curve can be found in Fig. B.7. Posterior distributions of key stepping parameters for TOI-5699 can be found in Fig. B.15.

4.3. TOI-2158

As seen in the periodogram for TOI-2158 in Fig. 5 and as is clearly visible in the time series in Fig. B.13, there seems to be multiple signals in the RVs. We therefore tested a suite of models starting from a model that only included just one Keplerian orbit and all the way up to three with linear and quadratic trends in between. For all of these runs, the eccentricity was allowed to vary for planet b and c (when included); however, for the

Table 3. The ΔBIC between the setup preffered by the data (3 Keplerians) and the different tests for TOI-2158 system.

Model	ΔBIC
1 Keplerian	248.91
1 Keplerian + lin. trend	109.55
1 Keplerian + quad. trend	107.45
2 Keplerians	223.26
2 Keplerians + lin. trend	59.87
2 Keplerians + quad. trend	15.94
3 Keplerians	0.00

three Keplerian cases, we fixed $e = 0$ for planet d as we had not yet covered a full orbit and so, e is thus difficult to constrain. The setup was otherwise identical to that outlined above and we performed MCMC sampling for all of these.

As for TOI-5699, we calculated the ΔBIC from each of these runs. The ΔBIC between each of these and the preferred model are summarised in Table 3. The preferred model is the three Keplerian model.

In this preferred setup, the eccentricities for the orbits of planet b and c came out to $e_b = 0.028^{+0.013}_{-0.014}$ and $e_c = 0.54 \pm 0.04$, respectively. Planet c is on a quite eccentric orbit, whereas e_b is consistent with zero. We further investigated whether a circular orbit for planet c would be preferred in this setup, but the difference in BIC was ΔBIC = 52.94 in favour of the eccentric solution. We also tried to let the eccentricity of planet d vary, while applying a Gamma prior (as we tried for TOI-5699). We found that adding the two extra parameters (e, ω) was not preferred over fixing e to zero. Our final setup is therefore a three-planet model in which the orbital eccentricities for planet b and c are allowed to vary, while fixing $e = 0$ for planet d.

Despite the fact that it does not cover a full cycle, the orbital period of planet d is determined quite well, 3336^{+378}_{-538} d, although we note that the posteriors in Fig. B.18 show long tails towards longer orbital periods and larger K-amplitudes. When allowing the eccentricity to vary, these tails can be stretched out even further. Furthermore, we gave more weight to shorter orbital periods and K-amplitudes by in stepping the logarithm of P and K. Finally, we note that the preference for a three planet Keplerian over a two planet model including a quadratic trend came just after adding the latest TS23 datum acquired on 2026-01-26. Further monitoring will establish if the proposed curvature is indeed accurate, which ultimately affects the derived orbital period and minimum mass for this companion.

In Fig. 4, we show the phase-folded TESS light curve of planet b with the best-fitting model. The ground-based light curves can be seen in Fig. B.8. In Figs. 8, 9, and 10, the best-fitting RV models for planet b, c, and d, respectively, are shown. Parameters for all planets are given in Table 4. Posterior distributions of the orbital parameters for each planet can be found in Figs. B.16, B.17, and B.18.

5. Discussion

To place our systems in context, we compiled a comparison sample of known giant planets. We queried the `pscomppars` table from the NASA Exoplanet Archive (NEA Akeson et al. 2013; Christiansen et al. 2025) on 2026-06-23. We replace eccentricities, whenever possible, with values from Bonomo et al. (2017), who provided homogeneous eccentricity determinations

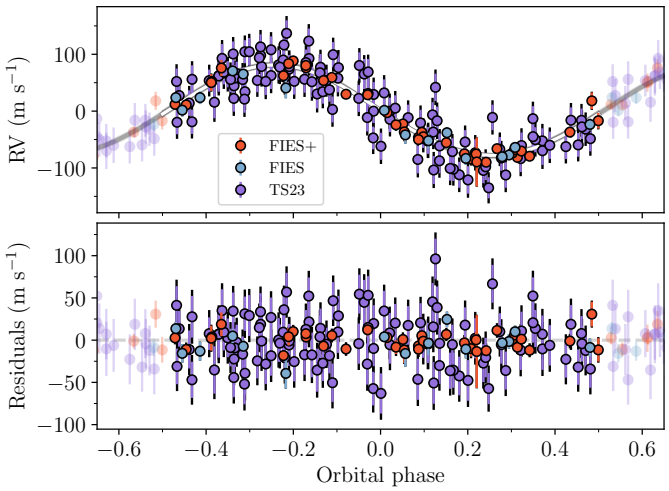


Fig. 8. RV curve for TOI-2158 b. RVs from TS23 are shown with purple markers, FIES+ RVs are shown with orange, and light blue markers demarcate FIES observations. The best-fitting RV curve for TOI-2158 b is overplotted after subtracting the modulation from planet c and the long-term trend. The grey shaded regions show the 1 and 2σ confidence intervals.

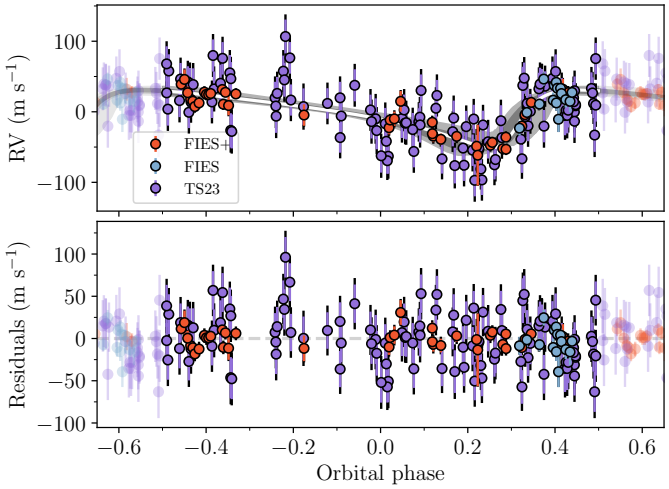


Fig. 9. Same as in Fig. 8 but for TOI-2158 c.

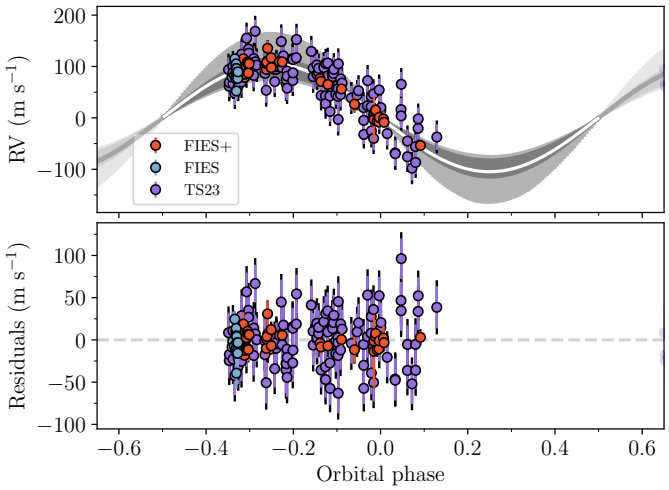


Fig. 10. Same as in Fig. 8 but for TOI-2158 d.

Table 4. Posterior values from the joint fit of the RVs and TESS photometry for the three systems.

	TOI-5120	TOI-5699	TOI-2158
		Planet b	
T_0 (BJD_{TDB})	2460267.9303 ± 0.0003	2459704.1558 ± 0.0009	2459018.9195 ± 0.0008
P (d)	24.91645 ± 0.00002	22.01850 ± 0.00004	$8.60079^{+0.00002}_{-0.00001}$
$a/R_\star$	26.1 ± 1.0	21^{+2}_{-3}	11.5 ± 0.4
$\cos i$	$0.014^{+0.004}_{-0.003}$	$0.055^{+0.012}_{-0.015}$	0.074 ± 0.004
$R_p/R_\star$	0.0703 ± 0.0005	0.0624 ± 0.0012	0.0702 ± 0.0007
K (m s^{-1})	79.6 ± 2.0	$16.9^{+1.8}_{-1.7}$	79.8 ± 1.8
$\sqrt{e}\cos\omega$	$0.21^{+0.04}_{-0.03}$	-0.02 ± 0.16	$0.12^{+0.05}_{-0.04}$
$\sqrt{e}\sin\omega$	$0.24^{+0.06}_{-0.05}$	$0.53^{+0.09}_{-0.08}$	$0.06^{+0.12}_{-0.09}$
e	0.10 ± 0.02	$0.30^{+0.09}_{-0.08}$	$0.028^{+0.013}_{-0.014}$
ω (°)	49^{+12}_{-10}	92^{+18}_{-17}	26^{+46}_{-35}
i (°)	$89.20^{+0.18}_{-0.21}$	$86.9^{+0.9}_{-0.7}$	$85.8^{+0.3}_{-0.2}$
b	$0.34^{+0.08}_{-0.06}$	$0.82^{+0.04}_{-0.03}$	$0.840^{+0.012}_{-0.011}$
d	$0.39^{+0.10}_{-0.07}$	1.5 ± 0.3	0.85 ± 0.03
T_{41} (hr)	6.87 ± 0.03	$3.95^{+0.10}_{-0.09}$	3.77 ± 0.04
T_{21} (hr)	0.51 ± 0.03	$0.65^{+0.12}_{-0.13}$	0.75 ± 0.06
R_p (R_J)	0.969 ± 0.017	0.996 ± 0.015	0.899 ± 0.015
M_p (M_J)	1.23 ± 0.05	0.25 ± 0.03	0.87 ± 0.04
T_{eq} (K)	796 ± 18	906 ± 55	1173 ± 23
a (AU)	0.172 ± 0.007	0.160 ± 0.019	0.070 ± 0.002
F ($F_\oplus$)	66 ± 6	112 ± 10	215 ± 15
TSM	17.4 ± 1.7	77 ± 12	36 ± 3
ESM	14.9 ± 0.9	14.5 ± 1.8	38.1 ± 1.7
			Planet c / Planet d
T_0 (BJD_{TDB})	···	···	2459620^{+18}_{-14} / 2460505^{+81}_{-115}
P (d)	···	···	$414.5^{+1.5}_{-1.6}$ / 3336^{+378}_{-538}
K (m s^{-1})	···	···	41 ± 3 / 91^{+11}_{-16}
$\sqrt{e}\cos\omega$	···	···	$-0.37^{+0.09}_{-0.10}$ / 0
$\sqrt{e}\sin\omega$	···	···	$-0.64^{+0.07}_{-0.08}$ / 0
e	···	···	0.54 ± 0.04 / 0
ω (°)	···	···	-120 ± 9 / 90
$M_p \sin i$ (M_J)	···	···	1.62 ± 0.13 / 7.2 ± 1.1
$a \sin i$ (AU)	···	···	0.95 ± 0.08 / 4.5 ± 0.7
		System/instrument	
γ_1 (m s^{-1})	47781 ± 2	$65122.9^{+1.5}_{-1.2}$	-64817^{+18}_{-12}
γ_2 (m s^{-1})	$38.7^{+1.8}_{-1.7}$	-45^{+4}_{-3}	-35^{+21}_{-16}
γ_3 (m s^{-1})	···	···	-40^{+17}_{-12}
ς_1 (m s^{-1})	13 ± 3	$0.006^{+0.027}_{-0.006}$	20 ± 3
ς_2 (m s^{-1})	$0.02^{+0.24}_{-0.02}$	$0.007^{+0.027}_{-0.007}$	$0.3^{+3.0}_{-0.3}$
ς_3 (m s^{-1})	···	···	$6.7^{+1.5}_{-1.7}$

Notes. Values immediately below the dashed lines are derived from the posterior samples. T_0 is the mid-transit time, P is the orbital period, $a/R_\star$ is the semi-major axis scaled by the stellar radius, i is the orbital inclination, $R_p/R_\star$ is the planet-to-star radius ratio, K is the RV semi-amplitude, e is the eccentricity, ω is the argument of periastron, b is the transit impact parameter, d is the occultation impact parameter, T_{41} and T_{21} are the full and ingress/egress durations, R_p is the planet radius, M_p is the planet mass, ρ_p is the planet density, T_{eq} is the equilibrium temperature, a is the semi-major axis, F is the insolation. TSM and ESM are the transmission and emission spectroscopy metrics, respectively (Eqs. (1) and (4) in Kempton et al. 2018). γ is the RV offset and ς is the RV jitter. The subscripts 1, 2, and 3 refer to TS23, FIES+, and FIES.

for transiting giant planets based on a combined analysis of radial velocities and transit data.

5.1. System architectures and properties

The TOI-5120 system consists of a Jupiter-like planet ($R_p = 0.969 \pm 0.017$ R_J, $M_p = 1.23 \pm 0.05$ M_J) on a wide orbit ($a/R_\star = 26.1 \pm 1.0$, $a = 0.172 \pm 0.007$ AU) and a likely stellar companion, which we have detected at a separation of 1.26″ (~290 AU). The orbit of TOI-5120 b is slightly eccentric at $e = 0.10 \pm 0.02$.

TOI-5699 is another warm Jupiter system ($a/R_\star = 21^{+2}_{-3}$, $a = 0.160 \pm 0.019$ AU, $R_p = 0.996 \pm 0.015$ R_J, $M_p = 0.25 \pm 0.03$ M_J), but unlike for the other two systems we detect no companions. For the orbit of TOI-5699 b we measure a modest, but significant eccentricity of $e = 0.30^{+0.09}_{-0.08}$. Although again we note that we cannot unambiguously rule out a circular orbit.

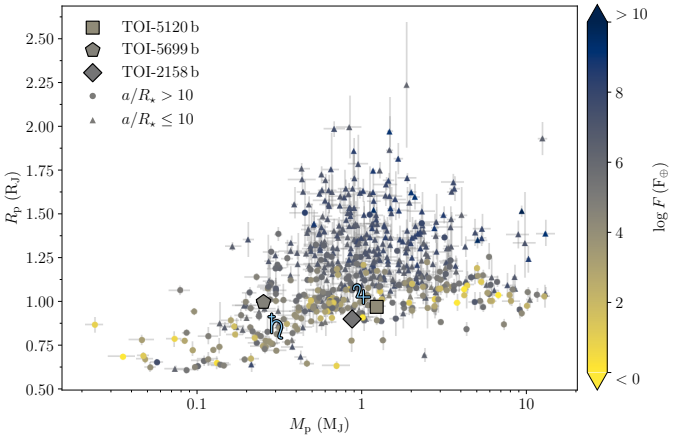


Fig. 11. Mass-radius diagram for giant planets defined as $M_p < 13$ M_J and ($M_p > 0.3$ M_J or $R_p > 0.6$ R_J) with mass and radius measurements more precise than 20%. Triangles denote hot Jupiters and warm Jupiters are shown with circles. Markers are colour-coded according to the insolation. The locations of Jupiter and Saturn are shown with their respective symbols.

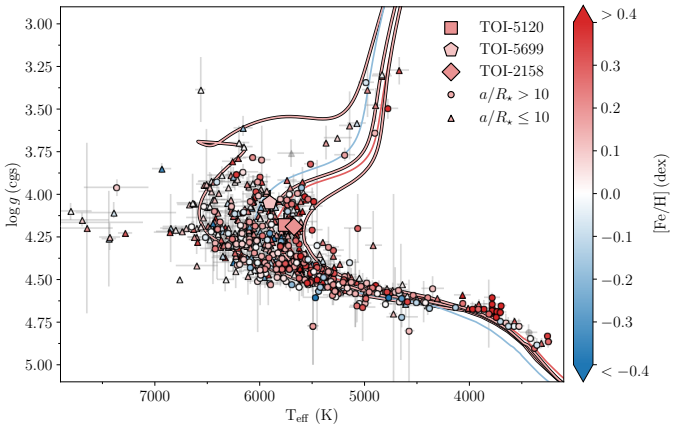


Fig. 12. Kiel diagram for the host stars in Fig. 11. Warm Jupiter systems ($a/R_\star > 10$) are shown with circles and hot Jupiter systems with (slightly transparent) squares. Stars are colour-coded according to their metallicity. We show three BaSTI isochrones (with the inclusion of diffusion, mass loss, and overshooting) at [Fe/H] = 0.15 with ages (from left to right) of 2 Gyr, 7 Gyr, and 13 Gyr. We furthermore show two additional 7 Gyr isochrones with [Fe/H] = −0.08 and [Fe/H] = 0.3.

TOI-2158 b is a Jupiter-sized planet ($R_p = 0.899 \pm 0.015$ R_J, $M_p = 0.87 \pm 0.04$ M_J) orbiting a slightly evolved G-type star in a system with potentially two outer companions. The planet is at the border between being a warm Jupiter ($a/R_\star = 11.5 \pm 0.4$, $a = 0.160 \pm 0.019$ AU) if the distinction is made in $a/R_\star$ with $a/R_\star > 10$ typically denoting warm Jupiters, or a hot Jupiter ($P = 8.60079^{+0.00002}_{-0.00001}$ d) when considering the orbital period, where the distinction is typically made at $P = 10$ d, although Dong et al. (2021a); Fairnington et al. (2026) use $P > 8$ d for warm Jupiters. We therefore refer to TOI-2158 b as a warm Jupiter. TOI-2158 c is likely a Jupiter-mass planet ($M_p \sin i = 1.62 \pm 0.13$ M_J) with an orbital period of $414.5^{+1.5}_{-1.6}$ d. The orbit of planet c is quite eccentric ($e = 0.54 \pm 0.04$), whereas the orbit of planet b is consistent with being circular ($e = 0.028^{+0.013}_{-0.014}$). For the outermost companion we have so far only detected a long-term trend and have not yet covered a full orbit. Nonetheless, a three-planet model is statistically preferred over a two-planet model plus a quadratic trend. Assuming a Keplerian model for this outer signal yields an orbital period of 3336^{+378}_{-538} d and a K-amplitude of 91^{+11}_{-16} m s^{-1}, which would (most likely) make it a planetary object (with $M_p \sin i = 7.2 \pm 1.1$ M_J assuming $e = 0$).

In Fig. 11, we show a radius-mass diagram of giant planets defined as planets larger than 0.6 $R_J$or more massive than 0.3 $M_J$and in both cases less massive than 13 M_J. We furthermore only show planets with masses and radii determined to better than 20%. The three transiting planets from this study are highlighted. In terms of size and mass, TOI-5120 b and TOI-2158 b are archetypical Jupiters with values very close to that of Jupiter. While the size of TOI-5699 b is similar to that of Jupiter and the two other planets, it is significantly less massive and more comparable to Saturn in mass. Dividing the planets into either hot or warm giants using $a/R_\star$ below or above 10 in Fig. 11 clearly illustrates the radius inflation often observed for hot Jupiters

The three host stars are quite similar in terms of T_{eff}, log $g_\star$, and [Fe/H], and they are all slightly evolved. The Kiel diagram in Fig. 12 shows that among stars hosting transiting, warm Jupiters, these three do indeed belong to the more evolved segment. In this context, it is of course also worth noting that as a star evolves and expands, $a/R_\star$ shrinks (for constant/decreasing a) and a warm Jupiter could transition to a hot Jupiter (given the $a/R_\star$ distinction).

Figure 12 also shows the well-known correlation that giant planets are more frequently found around stars with super solar metallicity (e.g. Fischer & Valenti 2005; Sousa et al. 2011) as is the case for the three systems investigated here. This trend is commonly interpreted as evidence that metal-rich protoplanetary discs are more efficient at forming the solid cores required for the subsequent accretion of massive gaseous envelopes.

5.2. Formation and migration

The formation of a hot Jupiter is generally ascribed to one of three mechanisms; in-situ formation, disc migration, or high-eccentricity (high-e) tidal migration. As the name implies, in situ formation offers a straightforward explanation. The giant planet would form at the observed separation either through gravitational instability or through core accretion. However, both of these formation channels have their limitations in forming these massive planets at these small orbital separation (e.g. Rafikov 2005; Schlichting 2014; Dawson & Johnson 2018). If we do not believe these planets to be able form at the observed locations, they must naturally have been transported to their current location in some way.

In gas disc migration the semi-major axis shrinks as the planet exchanges angular momentum with the gas and dust particles in the protoplanetary disc, which implies that through this channel migration takes place within the lifetime of the disc (i.e. within the first ∼10 Myr of the system). Disc migration can effectively shrink the orbit from several AU to just a few hundredths of an AU (e.g. Lin et al. 1996). It is typically considered a quiet form of migration in that both the eccentricity and obliquity remain low (i.e. the planet is found on a close to circular orbit that is well-aligned with the stellar spin axis; Duffell & Chiang 2015).

In contrast, high-e migration can excite both eccentricities and obliquities to large values. This happens when a perturber reduces the orbital angular momentum of a Jupiter by placing it on a highly elliptical orbit, either through planet-planet scattering (e.g. Rasio & Ford 1996) or secular interactions such as von

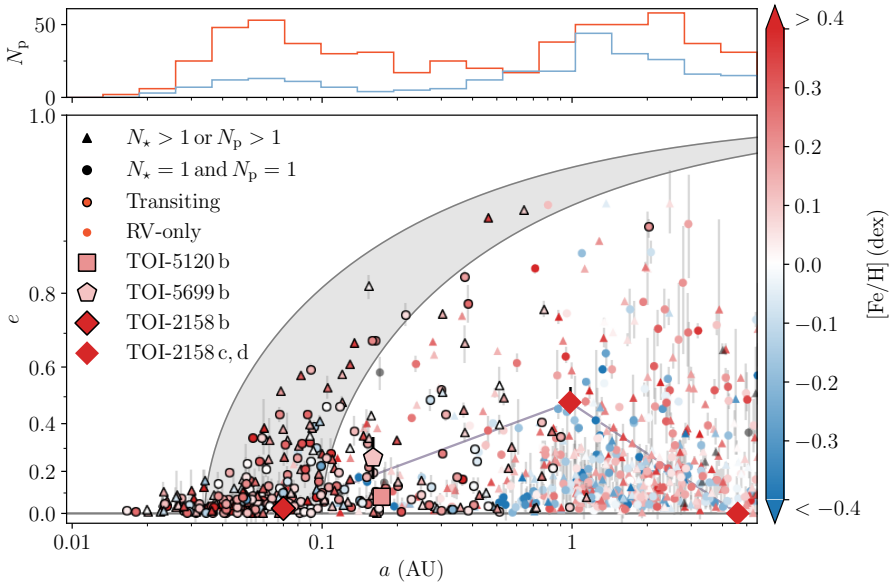


Fig. 13. Eccentricities of giant planets plotted against their semi-major axis. Markers with a black outline are transiting planets with the same criteria as in Fig. 11 and well-constrained eccentricities. Markers without a black outline are giant planets discovered through RV in the same mass range and well-constrained eccentricities. Marker shapes denote whether the system is a multistar system ($N_\star > 1$), a multiplanet system ($N_p > 1$), or both, or whether it is a single star, single planet system (as given in the NEA). As in Fig. 12, markers are colour-coded according to host star metallicity. The grey shaded area shows where one might expect planets undergoing high-e tidal migration. The y-axis is linear in $1 - e^2$. Histograms for the number of planets in a given semi-major axis bin are shown on top for host stars with super-solar metallicities ([Fe/H] > 0.0) in red and sub-solar in blue. Adapted from Dawson & Johnson (2018) and Dong et al. (2021b).

Zeipel-Kozai-Lidov (ZKL; von Zeipel 1910; Kozai 1962; Lidov 1962) oscillations driven by outer planetary or stellar companions (e.g. Wu & Murray 2003). Orbital energy might then be removed as the planet is stretched by the star during the close passages during periapsis (Fabrycky & Tremaine 2007). This tidal dissipation phase shrinks and circularises the orbit with a final semi-major axis given by $a_{\rm final} = a(1 - e^2)$, which for $e \to 1$ becomes $a_{\rm final} \approx 2a(1 - e)$, meaning that the initial periastron is $\approx \frac{1}{2} a_{\rm final}$.

As high-e migration can take place throughout the system's lifetime that also implies that we could catch planets in transition, i.e. giant planets on wide orbits with extreme eccentricity undergoing tidal migration and circularisation. The transition timescale for going from cold to hot, however, has been suggested to be short compared to the time spent as a cold Jupiter (Anderson & Lai 2017), and catching planets en route might therefore be difficult. Nonetheless, in Fig. 13 these proto hot Jupiters would be found in the grey shaded region in Fig. 13, which is bounded by tracks of constant angular momentum. As planets would be tidally disrupted as they pass inside the Roche limit, $a_{\rm Roche} \approx f_p R_p (M_p/M_\star)^{(1/3)}$ (where f_p is a dimensionless coefficient we assume to be 2.7; Guillochon et al. 2011), $a_{\rm final}$ must therefore be greater than $2a_{\rm Roche}$. For a 1 M_J, 1.3 R_J planet orbiting a solar-mass star (as used in Dong et al. 2021b) this comes out to 0.034 AU. As tidal circularisation depends critically on the orbital separation, the lower limit is taken as $a_{\rm final} = 0.1$ AU, beyond which tidal migration is not expected on meaningful timescales (Dawson & Johnson 2018).

Some handy examples of potential hot Jupiter progenitors are the transiting, warm Jupiters HD 80606 b (Naef et al. 2001), TOI-3362 b (Dong et al. 2021b), and TIC 241249530 b (Gupta et al. 2024) seen in Fig. 13 as the three most eccentric planets in the grey region. TOI-2158 b is found well within these boundaries on a close-in orbit with virtually no eccentricity. Considering that we have detected two outer companions, with the inner companion of those two found on a quite eccentric orbit, high-e tidal migration therefore provides a plausible evolutionary pathway for TOI-2158 b. However, the present-day architecture does not uniquely establish such a history, and alternative scenarios, such as migration through the protoplanetary disc followed by subsequent excitation of the outer planets, cannot be ruled out. TOI-5120 b and TOI-5699 b are clearly not found within this region and do therefore not appear to be hot Jupiters in the making.

In addition to the systems mentioned above, in Fig. 13, we also show all transiting, giant planets again defined as $M_p < 13$ M_J and ($M_p > 0.3$ M_J or $R_p > 0.6$ R_J), although we do not require a certain precision in mass or radius as in Fig. 11. We do, however, only include planets with well-constrained eccentricities, namely planets with e constrained to better than 50% or with uncertainties less than 0.2 for planets with $e < 0.2$ (Dong et al. 2021b). Furthermore, we show planets detected through RV measurements in the same mass range ($M_p \sin i$ from 0.3 to 13 M_J) and invoking the same eccentricity constraints. The inclusion of these RV planets adds a lot of cold Jupiters to the sample, which clearly illustrates a dip in the number of planets per log interval at warm Jupiter separations, the so-called period valley (e.g. Jones et al. 2003; Udry et al. 2003).

5.2.1. Warm Jupiter eccentricity distribution

As for hot Jupiters, warm Jupiters are thought to form through one of the three aforementioned mechanisms. Another issue with invoking in situ formation is that many warm Jupiters have been observed to display rather high eccentricities ($e \gtrsim 0.2$). This high-e component for the distribution also poses a problem in gas disc migration as planet-planet scattering at these separations tends to lead to collisions rather than eccentricity excitation (Petrovich et al. 2014). On the other hand, the low-e component is difficult to account for if warm Jupiters form through high-e migration. The eccentricity distribution of warm Jupiters thus comprises both low- and high-e components, both of which must be reproduced by theoretical models and properly considered when inferring the functional form of the observed distribution.

Owing to their flexibility with only two shape parameters, the Gamma and Beta distributions (mentioned in Sect. 4) are popular choices for modelling the exoplanet eccentricity distribution in general, with the added benefit for the latter that its domain is restricted to [0, 1] (e.g. Kipping 2013). The Beta distribution has been used extensively as a prior when fitting the eccentricity, especially in low S/N cases, or it has been used for populations syntheses, for instance, as done in Sect. 5.2.2.

Physically motivated distributions include the mixture of the Exponential distribution and the Rayleigh distribution, where the

former should capture the planets undergoing tidal dissipation (Rasio & Ford 1996) and the latter should reflect the outcome of planet-planet scattering (Jurić & Tremaine 2008). In the high-e tidal migration scenario, this mixture model should therefore nicely account for the observed distribution. Stevenson et al. (2025, $\mathcal{RE}$ in their notation) found that this model was the preferred distribution (among those investigated) when considering all planets discovered with radial velocities.

Accordingly, we investigated the warm Jupiter eccentricity distribution using hierarchical Bayesian modelling (HBM). We created the HBM and sampled the posterior using `PyMC` (Abril-Pla et al. 2023). We modelled each planet's latent eccentricity as drawn from a two-component mixture on $[0, 1]$: a truncated Exponential distribution and a truncated Rayleigh distribution, mixed with weight, α, which can then be interpreted as the fraction of systems consistent with tidal damping versus dynamical excitation. Truncation is needed (as noted by Kipping 2013; Stevenson et al. 2025) since a problem with the $\mathcal{RE}$ distribution is that it assigns a non-zero probability to hyperbolic orbits. We placed weakly informative hyperpriors on the parameters of mixture model: $\alpha \sim \text{Beta}(1, 1)$, $\ln\sigma \sim \text{Uniform}(-8, 3)$, and $\ln\lambda \sim \text{Uniform}(-5, 5)$, where $\sigma = \exp(\ln\sigma)$ and $\lambda = \exp(\ln\lambda)$ are the shape parameters for the Rayleigh respectively Exponential distribution. Observed eccentricities are modelled with Gaussian measurement errors around latent eccentricities: $e_i^{\text{obs}} \sim \mathcal{N}(e_i, s_i^2)$, where s_i is the reported 1σ uncertainty (floored at 10^{-4} for numerical stability).

We defined our sample of warm Jupiters as those planets meeting the criteria used to create Fig. 13, but only including planets with orbital periods between 8 and 200 d as in (Dong et al. 2021b; Fairnington et al. 2026, roughly between 0.08 and 0.67 AU), thereby also conveniently including TOI-2158 b. A histogram for the eccentricities of these $N = 188$ planets are shown in Fig. 14, where we also compare our sample to the ($N = 891$) sample of eccentricities from RV detected planets used in Stevenson et al. (2025). Clearly, our sample is characterised by a greater number of low-eccentricity planets compared to theirs, possibly owing to the inclusion of more close-in planets, which might have tidally circularised. From our HBM we do indeed also get a slightly larger contribution from the Exponential population with $\alpha = 0.77 \pm 0.06$ compared to $\alpha = 0.70 \pm 0.02$ in Stevenson et al. (2025). For the shape parameters we get $\lambda = 3.1 \pm 0.5$ and $\sigma = 0.029 \pm 0.006$ ($\lambda = 3.39^{+0.09}_{-0.10}$, $\sigma = 0.111 \pm 0.003$ in Stevenson et al. 2025). Although employing different models, by fitting a Beta distribution to the eccentricities of transiting warm Jupiters with orbit periods between 10 and 1000 days, Gan et al. (2025) also found that most warm Jupiters exhibit circular orbits (shape parameters of $\alpha = 0.64 \pm 0.07$ and $\beta = 1.55 \pm 0.12$).

As mentioned, the overall occurrence rate of giant planets correlates with stellar metallicity, and we might therefore also expect planet-planet interactions (through scattering or ZKL oscillations) to occur more frequently in such systems. This in turn could thus be reflected in the relative contributions to the $\mathcal{RE}$ mixture model when comparing the eccentricities of planets around stars at either sub- or super-solar metallicity. This effect might naturally also be visible more directly when comparing the eccentricities of planets with confirmed outer companions to those without. Slicing and dicing the sample of eccentricities of warm Jupiters has been done in various ways, where, for instance, Dong et al. (2014) reported that the fraction of warm Jupiters with outer companions ("jovian perturbers") was an increasing function of eccentricity as opposed to those without companions, and Morgan et al. (2026) recently found that

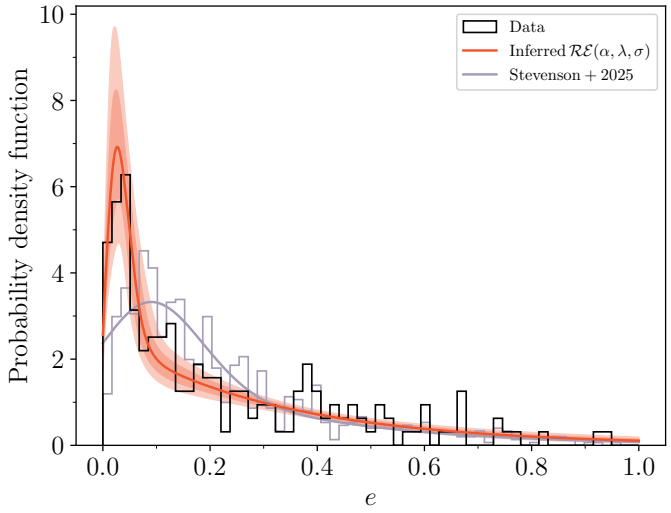


Fig. 14. Shown in black is our sample of warm Jupiter eccentricities. In red, we show the Rayleigh+Exponential distribution resulting from our HBM with parameters $\alpha = 0.77 \pm 0.06$, $\lambda = 3.1 \pm 0.5$, and $\sigma = 0.029 \pm 0.006$. In grey we show the RV eccentricity sample from Stevenson et al. (2025) along with their Rayleigh+Exponential distribution.

warm Jupiters orbiting metal-rich stars have higher eccentricities compared to those around metal-poor stars.

To see if the physically motivated distributions might reveal more about the preferred migration channel, we tried splitting our warm Jupiter sample into systems with companions, with no distinction on the type of companion ($N_\star > 1$ or $N_{\text{pl}} > 1$), and those without ($N_\star = 1$ and $N_{\text{pl}} = 1$). From this we found $\alpha = 0.66 \pm 0.09$ for the systems with companions and $\alpha = 0.87 \pm 0.07$ for those without, indicating that dynamically excited orbits are more prevalent in systems with companions, consistent with scattering or secular perturbations driving eccentricity growth.

We also tried to investigate the correlation between metallicity and eccentricity, but instead of dividing the sample into two (or more) rather arbitrary bins, for instance, a super- and sub-solar [Fe/H]-population, we modelled the mixture weight as a function of host-star metallicity. Specifically, for each planet i we define the Rayleigh weight α_i via a logistic (sigmoid) link function $\text{logit}(\alpha_i) \equiv \ln\frac{\alpha_i}{1-\alpha_i} = \beta_0 + \beta_1[\text{Fe/H}]_i$, meaning that

$$\alpha_i = \frac{1}{1 + e^{-(\beta_0 + \beta_1[\text{Fe/H}]_i)}}, \tag{2}$$

where β_0 sets the intercept of the population-averaged weight at solar metallicity, while the slope β_1 quantifies the metallicity dependence: $\beta_1 > 0$ implies that metal-rich systems are more likely to have eccentricities drawn from the Rayleigh distribution, consistent with dynamical excitation in metal-rich systems hosting giant planets. We placed weakly informative priors on $\beta_0, \beta_1 \sim \mathcal{N}(0, 2)$, which are broad on the logit scale and allow α_i to span the full range $(0, 1)$. To enforce physically meaningful component shapes (with the Exponential representing a near-circular population and the Rayleigh an excited one), we restricted $\lambda \in [3.3, 33]$, corresponding to a mean of $\langle e \rangle < 0.3$) and $\sigma \in [0.20, 0.82]$, so that the Rayleigh mode $e = \sigma > 0.2$. The crossover metallicity $[\text{Fe/H}]^* = -\beta_0/\beta_1$ marks where neither component is preferred ($\alpha_i = 0.5$). From this ,we found $\lambda = 13 \pm 3$, $\sigma = 0.33 \pm 0.04$, $\beta_0 = -0.5 \pm 0.4$, and $\beta_1 = 2.2 \pm 0.9$, which corresponds to a cross-over metallicity of $[\text{Fe/H}] = 0.22^{+0.22}_{-0.13}$.

This indicates that the Rayleigh distribution becomes dominant above [Fe/H] = 0.2.

We note that there are probably some uncertainties in the results presented here, given how the samples were constructed. First off, to properly investigate the influence of companions one should assess the relevance of these companions, meaning are they massive and/or nearby enough (and sufficiently inclined), for the proposed migration mechanisms, as well as the completeness for the systems without companions (i.e. what range in mass and orbital separation can be excluded; see Sect. 5.2.2). Secondly, we found that when modelling the mixture weight as a function of host-star metallicity using a logistic function, it was necessary to enforce the priors as outlined, indicating that the results are perhaps not as robust as desired. Furthermore, mixing samples of systems discovered through RV and transit also means mixing selection functions (e.g. the transit method is biased towards close-in and eccentric planets), which we do not attempt to mitigate here. We therefore do not necessarily expect our results to reflect the true underlying distributions of the different samples; these are simply the distributions obtained when considering the currently available systems that meet our selection criteria. Future constraints on outer companions and homogeneous samples will be key to determining whether the eccentricity distribution can robustly disentangle the dominant migration pathways of warm Jupiters.

5.2.2. Companions and completeness

The eccentricities for TOI-5120 b and TOI-5699 b appear to be too low for them to be undergoing high-e tidal migration. However, if (as of yet undetected) outer planetary companions reside in these systems, the inner planets might periodically have their eccentricity excited through secular interactions and during this high-e phase undergo tidal migration as suggested by Petrovich & Tremaine (2016). In this steady-state picture, the warm Jupiter spends most of its time at relatively low eccentricities. Moreover, if the eccentricity excitation is driven by ZKL cycles, the exchange between eccentricity and inclination implies that low-e phases may coincide with high mutual inclinations, which remain unconstrained for these systems. As a result, the currently observed low eccentricities do not necessarily rule out ongoing high-e tidal migration. As argued, although modest the eccentricity we do seem to measure for TOI-5699 b (assuming it is significant cf. Sect. 4.2) is difficult to account for in the in situ or disc migration scenarios, and as such this steady-state mechanism might offer an explanation.

In TOI-5120, we detected a stellar companion (physical separation ~300 AU), which might have triggered secular interactions and caused the planet to migrate, although we currently know very little about this companion and thus its possible influence. Furthermore, Petrovich (2015) found that stellar companions produced very few planets at separations intermediate to hot and cold Jupiters (~0.1 to 2 AU).

We therefore tried to place limits on potential planetary companions in these systems. In Fig. 15 we show the sensitivity limits in terms of mass and semi-major axis from our TS23 and FIES observations for TOI-5120 and TOI-5699. These plots have been created through injection and recovery tests given our data following the approaches in Bryan et al. (2019); Bonomo et al. (2023). The plots are evidently quite similar, since we have comparable baselines, number of observations, and root mean squares. Given our data, we are able to exclude Jupiter-mass planets out to a couple of AU.

In Fig. 15, we also show an approximation for the mass and semi-major axis a perturber would need to have to overcome general-relativistic precession (Eq. (14) in Dawson & Johnson 2018; see also Dong et al. 2014). A companion would therefore have to lie to the left of this line to excite the eccentricity of the inner planet. Efficient secular excitation further requires that the outer companion dominates the angular momentum budget of the system. In hierarchical systems the orbital angular momentum scales approximately as $L \propto M\sqrt{a}$, such that the ratio of inner to outer angular momentum is $L_{\rm in}/L_{\rm out} \sim (M_{\rm p,in}/M_{\rm p,out})\sqrt{a_{\rm in}/a_{\rm out}}$ (e.g. Liu et al. 2015). Therefore, a high eccentricity excitation would only be expected when the outer orbit carries a comparable or larger share of the total angular momentum, implying that perturbers capable of driving strong secular excitation are typically comparable to or more massive than the inner planet. Applying this constraint, as shown in Fig. 15, leaves only a narrow range in mass and semi-major axis for potential perturbers. While these constraints are admittedly somewhat "hand-wavy", they nevertheless illustrate that a companion capable of exciting the eccentricity of TOI-5120 b is unlikely. In contrast, for TOI-5699 b our current data still leave some room for a companion to remain undetected.

5.3. Future studies

Continued RV monitoring of TOI-5120 and TOI-5699 will provide even stronger constraints on the possible masses and orbital separations of potential outer companions or they might even reveal their presence. Additional RVs would also help constrain the eccentricity of TOI-5699 b further and determine whether the value we measure ($e = 0.30^{+0.09}_{-0.08}$) is not just (partly) an artifact of the current data. Continued RV monitoring of TOI-2158 is needed to cover a full orbit of the long-term trend and thereby determine the orbital period and minimum mass of the outer companion. As TESS continues to monitor the sky, more transits will be available for all three systems. Currently, TOI-2158 is slated to be observed in two sectors in June and July 2027.

All three (transiting) planets are amenable targets for measurements of the Rossiter–McLaughlin (RM; Rossiter 1924; McLaughlin 1924) effect. Using the simple approximation $0.7\sqrt{1-b^2}(R_{\rm p}/R_\star)^2 v \sin i_\star$, we calculated the amplitude for the RM anomaly to be 23 m s^{-1} for TOI-5120 b, 9 m s^{-1} for TOI-5699 b, and 10 m s^{-1} for TOI-2158 – well-within reach for many spectrographs. The relatively long duration of the transits ($\gtrsim$3.8 h) helps ensure proper sampling. As mentioned, dynamical interactions might also excite the obliquity of the host star, measurements of the RM effect would allow us to determine the projected obliquity and therefore help shed light on the dynamical histories in these systems. This is especially true for warm Jupiter systems as the larger orbital separation would minimise the effect of tidal realignment, which might erase this information (Albrecht et al. 2012).

We estimated the expected astrometric signal of TOI-2158 d following the standard reflex-motion relation. Given the minimum mass, orbital separation, and stellar mass (Tables 4 and 2), the induced stellar semi-major axis is $a_\star = a(M_{\rm p}/M_\star) \sim 0.03$ AU. At a distance of 198.5 ± 1.4 pc this translates to an astrometric signature of ~151 μas. This is several times larger than *Gaia*'s expected astrometric precision for stars with magnitudes of $G \sim 10$–11 (tens of μas; Perryman et al. 2014). Given the orbital period we find of 3336^{+378}_{-538} d, it might be possible to detect the wobble from TOI-2158 d in future *Gaia* data releases.

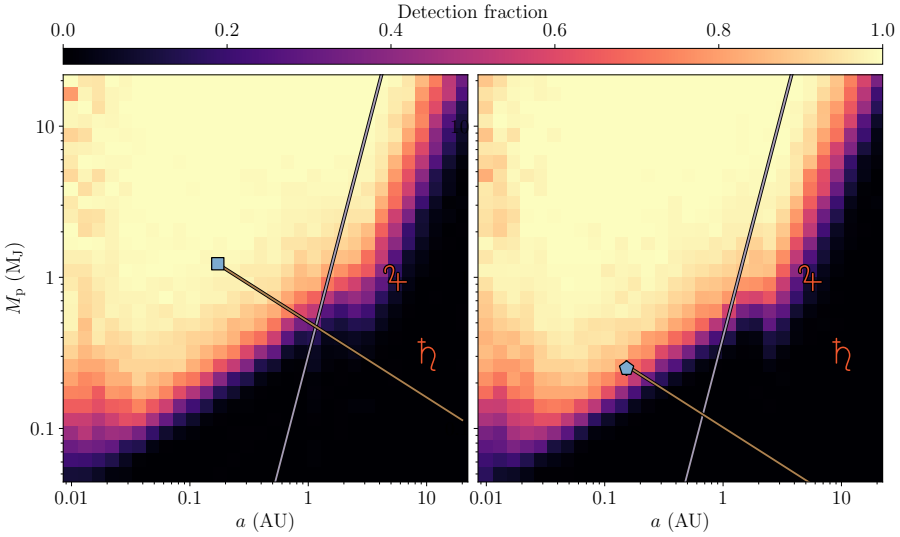


Fig. 15. Completeness maps from our RV observations of TOI-5120 (*left*) and TOI-5699 (*right*). The position of the transiting planets are shown with the blue markers and the position of Jupiter and Saturn are shown for reference. Each cell represents 300 planets with values drawn uniformly in cos i from 0 to 1 and ω between 0 and 2π with e drawn from a Beta distribution (Kipping 2013). The cell is then colour-coded according to the fraction of significantly detected signals (ΔBIC > 10). The grey line shows the minimum perturber mass required to overcome general-relativistic precession, while the brown line indicates where the outer companion dominates the system's angular momentum.

Such an astrometric detection would provide the orbital inclination and true mass of TOI-2158 d, and enable measurement of the mutual inclination between planets b and d.

Another piece of the puzzle could come from probing the atmospheres of these warm Jupiters, where, for instance, the C/O ratio might be able to trace the dynamical history and evolution (e.g. Madhusudhan et al. 2014). As discussed in relation to the CHEOPS observations of TOI-5120, this planet has already been identified as a potentially interesting target for the Ariel mission, although its transmission and emission spectroscopy metrics (TSM and ESM; Table 4) are comparatively modest. TOI-5699 b is the most favorable target for transmission spectroscopy, with a TSM of 77 ± 12, owing primarily to its low mass and consequently large atmospheric scale height. In contrast, TOI-2158 b has the highest ESM (38.1 ± 1.7), reflecting its higher equilibrium temperature and making it the most favorable target of the three for emission spectroscopy.

6. Conclusion

We report on the discovery and characterisation of two new transiting warm Jupiters, TOI-5120 b and TOI-5699 b. We sought to refine the parameters of the previously discovered warm Jupiter TOI-2158 b. All three planets are in orbit around slightly evolved, metal-rich host stars and all three have radii that are comparable to that of Jupiter, while spanning a range in masses and orbital architectures. In addition to the transiting planet, we detected an outer planetary companion in the TOI-2158 system and identified a long-term RV trend, potentially indicating the presence of an additional planetary companion on a wide orbit.

The three systems illustrate the diversity of warm Jupiter architectures. TOI-5120 b resides in a system with a likely wide stellar companion, while TOI-5699 b currently shows no evidence of any additional companions within the sensitivity of our RV observations. The TOI-2158 system, on the other hand, hosts multiple companions, including the eccentric outer planet TOI-2158 c and a possible additional distant body. These configurations highlight the range of dynamical environments in which warm Jupiters are found.

The modest eccentricities measured for TOI-5120 b and TOI-5699 b suggest that they are unlikely to be undergoing high-eccentricity tidal migration at present, although undetected companions could still actively excite their eccentricities through secular interactions. In contrast, the architecture of the TOI-2158 system, with an eccentric outer companion and indications of an additional perturber, is consistent with a dynamically active environment that could have influenced the migration history of the inner planet.

More broadly, these systems add to the growing sample of well-characterised warm Jupiters and contribute to population-level studies of their dynamical properties. As warm Jupiters are expected to retain signatures of their formation and migration histories, expanding this sample is essential for disentangling the relative roles of in situ formation, disc migration, and high-e tidal migration. Continued RV monitoring and measurements of the RM effect for these systems will further constrain their dynamical architectures and provide additional insights into the origins of warm Jupiters.

Data availability

Table A.2 is available at the CDS via https://cdsarc.cds.unistra.fr/viz-bin/cat/J/A+A/714/A496.

Acknowledgements. We thank the anonymous reviewer for valuable comments that helped improve the quality of the manuscript. This work was supported by a research grant (42101) from VILLUM FONDEN. DRC acknowledges partial support from NASA Grant 18-2XRP18_2-0007. This paper includes data taken at The McDonald Observatory of The University of Texas at Austin supported by the NASA grant 80NSSC23K0429. This study is based on observations made with the Nordic Optical Telescope, owned in collaboration by the University of Turku and Aarhus University, and operated jointly by Aarhus University, the University of Turku and the University of Oslo, representing Denmark, Finland and Norway, the University of Iceland and Stockholm University at the Observatorio del Roque de los Muchachos, La Palma, Spain, of the Instituto de Astrofísica de Canarias. This paper includes data collected with the TESS mission, obtained from the MAST data archive at the Space Telescope Science Institute (STScI). Funding for the TESS mission is provided by the NASA Explorer Program. STScI is operated by the Association of Universities for Research in Astronomy, Inc., under NASA contract NAS 5–26555. This research has made use of the Exoplanet Follow-up Observation Program (ExoFOP; DOI: 10.26134/ExoFOP5) website, which is operated by the California Institute of Technology, under contract with the National Aeronautics and Space Administration under the Exoplanet Exploration Program. Based on observations obtained at the Hale Telescope, Palomar Observatory, as part of a collaborative agreement between the Caltech Optical Observatories and the Jet Propulsion Laboratory [operated by Caltech for NASA]. Some of the observations in the paper made use of the NN-EXPLORE Exoplanet and Stellar Speckle Imager (NESSI). NESSI was funded by the NASA Exoplanet Exploration Program and the NASA Ames Research Center. NESSI was built at the Ames Research Center

by Steve B. Howell, Nic Scott, Elliott P. Horch, and Emmett Quigley. This work has made use of data from the European Space Agency (ESA) mission *Gaia* (https://www.cosmos.esa.int/gaia), processed by the *Gaia* Data Processing and Analysis Consortium (DPAC, https://www.cosmos.esa.int/web/gaia/dpac/consortium). Funding for the DPAC has been provided by national institutions, in particular the institutions participating in the *Gaia* Multilateral Agreement. This work has made use of the VALD database, operated at Uppsala University, the Institute of Astronomy RAS in Moscow, and the University of Vienna. This work makes use of observations from the LCOGT network. Part of the LCOGT telescope time was granted by NOIRLab through the Mid-Scale Innovations Program (MSIP). MSIP is funded by NSF. The work of BS was conducted under the state assignment of Lomonosov Moscow State University. T.G. acknowledges financial support from the Agencia Estatal de Investigación of the Ministerio de Ciencia e Innovación MCIN/AEI/10.13039/501100011033 and the ERDF "A way of making Europe" through projects PID2021-125627OB-C32 and PID2024-158486OB-C32. This work is supported by the European Union (ERC AdvG SPEAR, GA 101200674). Funding for KB was provided by the European Union (ERC AdG SUBSTELLAR, GA 101054354). This research has made use of the Exoplanet Follow-up Observation Program (ExoFOP; DOI: 10.26134/ExoFOP5) website, which is operated by the California Institute of Technology, under contract with the National Aeronautics and Space Administration under the Exoplanet Exploration Program. This research has made use of NASA's Astrophysics Data System. The TESS light curves were extracted using Lightkurve (Lightkurve Collaboration 2018). This work made use of the following `Python` packages; NumPy (Harris et al. 2020), SciPy (Virtanen et al. 2020), Matplotlib (Hunter 2007), dynesty (Speagle 2020), Nested Sampling (Skilling 2004, 2006), corner (Foreman-Mackey 2016), kepler.py (Foreman-Mackey et al. 2021), and Astropy (Astropy Collaboration 2013, 2018, 2022).

References

Abril-Pla, O., Andreani, V., Carroll, C., et al. 2023, PeerJ Comput. Sci., 9
Adams, F. C., & Laughlin, G. 2006, ApJ, 649, 1004
Aguirre Børsen-Koch, V., Rørsted, J. L., Justesen, A. B., et al. 2022, MNRAS, 509, 4344
Akeson, R. L., Chen, X., Ciardi, D., et al. 2013, PASP, 125, 989
Albrecht, S., Winn, J. N., Johnson, J. A., et al. 2012, ApJ, 757, 18
Anderson, K. R., & Lai, D. 2017, MNRAS, 472, 3692
Astropy Collaboration (Robitaille, T. P., et al.) 2013, A&A, 558, A33
Astropy Collaboration (Price-Whelan, A. M., et al.) 2018, AJ, 156, 123
Astropy Collaboration (Price-Whelan, A. M., et al.) 2022, ApJ, 935, 167
Bennett, M., & Bovy, J. 2019, MNRAS, 482, 1417
Benz, W., Broeg, C., Fortier, A., et al. 2021, Exp. Astron., 51, 109
Blanco-Cuaresma, S., Soubiran, C., Heiter, U., & Jofré, P. 2014, A&A, 569, A111
Bonomo, A. S., Desidera, S., Benatti, S., et al. 2017, A&A, 602, A107
Bonomo, A. S., Dumusque, X., Massa, A., et al. 2023, A&A, 677, A33
Bovy, J. 2015, ApJS, 216, 29
Brown, T. M., Baliber, N., Bianco, F. B., et al. 2013, PASP, 125, 1031
Bruntt, H., Bedding, T. R., Quirion, P. O., et al. 2010, MNRAS, 405, 1907
Bryan, M. L., Knutson, H. A., Lee, E. J., et al. 2019, AJ, 157, 52
Buchhave, L. A., Latham, D. W., Johansen, A., et al. 2012, Nature, 486, 375
Christiansen, J. L., McElroy, D. L., Harbut, M., et al. 2025, PSJ, 6, 186
Ciardi, D. R., Beichman, C. A., Horch, E. P., & Howell, S. B. 2015, ApJ, 805, 16
Claret, A. 2018, A&A, 618, A20
Claret, A., Hauschildt, P. H., & Witte, S. 2013, A&A, 552, A16
Collins, K. 2019, in American Astronomical Society Meeting Abstracts, 233, American Astronomical Society Meeting Abstracts #233, 140.05
Collins, K. A., Kielkopf, J. F., Stassun, K. G., & Hessman, F. V. 2017, AJ, 153, 77
Dawson, R. I., & Johnson, J. A. 2018, ARA&A, 56, 175
Dekany, R., Roberts, J., Burruss, R., et al. 2013, ApJ, 776, 130
Djupvik, A. A., & Andersen, J. 2010, in Astrophysics and Space Science Proceedings, 14, Highlights of Spanish Astrophysics V, 211
Dong, S., Katz, B., & Socrates, A. 2014, ApJ, 781, L5
Dong, J., Huang, C. X., Dawson, R. I., et al. 2021a, ApJS, 255, 6
Dong, J., Huang, C. X., Zhou, G., et al. 2021b, ApJ, 920, L16
Doyle, A. P., Davies, G. R., Smalley, B., Chaplin, W. J., & Elsworth, Y. 2014, MNRAS, 444, 3592
Duffell, P. C., & Chiang, E. 2015, ApJ, 812, 94
El-Badry, K., Rix, H.-W., & Heintz, T. M. 2021, MNRAS, 506, 2269
Endl, M., Kürster, M., & Els, S. 2000, A&A, 362, 585
Fabrycky, D., & Tremaine, S. 2007, ApJ, 669, 1298
Fairnington, T. R., Dong, J., Huang, C. X., et al. 2026, ApJ, 1008, L6
Fischer, D. A., & Valenti, J. 2005, ApJ, 622, 1102
Foreman-Mackey, D. 2016, J. Open Source Softw., 1, 24
Foreman-Mackey, D., Hogg, D. W., Lang, D., & Goodman, J. 2013, PASP, 125, 306
Foreman-Mackey, D., Agol, E., Ambikasaran, S., & Angus, R. 2017, AJ, 154, 220
Foreman-Mackey, D., Luger, R., Agol, E., et al. 2021, J. Open Source Softw., 6, 3285
Frandsen, S., & Lindberg, B. 1999, in Astrophysics with the NOT, eds. H. Karttunen, & V. Piirola, 71
Furlan, E., Ciardi, D. R., Everett, M. E., et al. 2017, AJ, 153, 71
Fűrész, G. 2008, PhD thesis, University of Szeged, Hungary
Gaia Collaboration (Vallenari, A., et al.) 2023, A&A, 674, A1
Gan, T., Cadieux, C., Ida, S., et al. 2025, ApJ, 988, L78
Gandolfi, D., Parviainen, H., Deeg, H. J., et al. 2015, A&A, 576, A11
GRAVITY Collaboration (Abuter, R., et al.) 2019, A&A, 625, L10
Gray, D. F. 2005, The Observation and Analysis of Stellar Photospheres
Guerrero, N. M., Seager, S., Huang, C. X., et al. 2021, ApJS, 254, 39
Guillochon, J., Ramirez-Ruiz, E., & Lin, D. 2011, ApJ, 732, 74
Gupta, A. F., Millholland, S. C., Im, H., et al. 2024, Nature, 632, 50
Gustafsson, B., Edvardsson, B., Eriksson, K., et al. 2008, A&A, 486, 951
Harris, C. R., Millman, K. J., van der Walt, S. J., et al. 2020, Nature, 585, 357
Hartman, J. D., & Bakos, G. Á. 2016, Astron. Comput., 17, 1
Hayward, T. L., Brandl, B., Pirger, B., et al. 2001, PASP, 113, 105
Hidalgo, S. L., Pietrinferni, A., Cassisi, S., et al. 2018, ApJ, 856, 125
Høg, E., Fabricius, C., Makarov, V. V., et al. 2000, A&A, 355, L27
Howell, S. B., Everett, M. E., Sherry, W., Horch, E., & Ciardi, D. R. 2011, AJ, 142, 19
Huang, C. X., Vanderburg, A., Pál, A., et al. 2020, RNAAS, 4, 206
Hunter, J. D. 2007, Comput. Sci. Eng., 9, 90
Jackson, B., Greenberg, R., & Barnes, R. 2008, ApJ, 678, 1396
Jenkins, J. M., Twicken, J. D., McCauliff, S., et al. 2016, Proc. SPIE, 9913, 99133E
Jensen, E. 2013, Tapir: A web interface for transit/eclipse observability, Astrophysics Source Code Library [record ascl:1306.007]
Jofré, P., Heiter, U., & Soubiran, C. 2019, ARA&A, 57, 571
Jones, H. R. A., Butler, R. P., Tinney, C. G., et al. 2003, MNRAS, 341, 948
Jurić, M., & Tremaine, S. 2008, ApJ, 686, 603
Kempton, E. M.-R., Bean, J. L., Louie, D. R., et al. 2018, PASP, 130, 114401
Kipping, D. M. 2013, MNRAS, 434, L51
Knudstrup, E., Serrano, L. M., Gandolfi, D., et al. 2022, A&A, 667, A22
Kovács, G., Zucker, S., & Mazeh, T. 2002, A&A, 391, 369
Kozai, Y. 1962, AJ, 67, 591
Kreidberg, L. 2015, PASP, 127, 1161
Larsen, J. R., Rørsted, J. L., Aguirre Børsen-Koch, V., et al. 2025, A&A, 697, A153
Lidov, M. L. 1962, Planet. Space Sci., 9, 719
Lightkurve Collaboration (Cardoso, J. V. d. M., et al.) 2018, Lightkurve: Kepler and TESS time series analysis in Python, Astrophysics Source Code Library [record ascl:1812.013]
Lin, D. N. C., Bodenheimer, P., & Richardson, D. C. 1996, Nature, 380, 606
Lindegren, L., Bastian, U., Biermann, M., et al. 2021, A&A, 649, A4
Liu, B., Muñoz, D. J., & Lai, D. 2015, MNRAS, 447, 747
Lucy, L. B., & Sweeney, M. A. 1971, AJ, 76, 544
Madhusudhan, N., Amin, M. A., & Kennedy, G. M. 2014, ApJ, 794, L12
Mandel, K., & Agol, E. 2002, ApJ, 580, L171
Matteucci, F. 2021, A&A Rev., 29, 5
Maxted, P. F. L., Ehrenreich, D., Wilson, T. G., et al. 2022, MNRAS, 514, 77
McLaughlin, D. B. 1924, ApJ, 60, 22
McMillan, P. J. 2017, MNRAS, 465, 76
Morgan, M., Bowler, B. P., & Tran, Q. H. 2026, AJ, 171, 19
Morris, R. L., Twicken, J. D., Smith, J. C., et al. 2020, Kepler Data Processing Handbook: Photometric Analysis, Kepler Science Document KSCI-19081-003
Naef, D., Latham, D. W., Mayor, M., et al. 2001, A&A, 375, L27
Perryman, M., Hartman, J., Bakos, G. Á., & Lindegren, L. 2014, ApJ, 797, 14
Persson, C. M., Fridlund, M., Barragán, O., et al. 2018, A&A, 618, A33
Petrovich, C. 2015, ApJ, 799, 27
Petrovich, C., & Tremaine, S. 2016, ApJ, 829, 132
Petrovich, C., Tremaine, S., & Rafikov, R. 2014, ApJ, 786, 101
Piskunov, N., & Valenti, J. A. 2017, A&A, 597, A16
Rafikov, R. R. 2005, ApJ, 621, L69
Rasio, F. A., & Ford, E. B. 1996, Science, 274, 954
Rice, M., Wang, S., Wang, X.-Y., et al. 2022, AJ, 164, 104
Ricker, G. R., Winn, J. N., Vanderspek, R., et al. 2015, J. Astron. Telesc. Instrum. Syst., 1, 014003
Rossiter, R. A. 1924, ApJ, 60, 15
Ryabchikova, T., Piskunov, N., Kurucz, R. L., et al. 2015, Phys. Scr, 90, 054005
Schlichting, H. E. 2014, ApJ, 795, L15
Schönrich, R., Binney, J., & Dehnen, W. 2010, MNRAS, 403, 1829

Scott, N. J., Howell, S. B., Horch, E. P., & Everett, M. E. 2018, PASP, 130, 054502
Seager, S., & Mallén-Ornelas, G. 2003, ApJ, 585, 1038
Silva Aguirre, V., Davies, G. R., Basu, S., et al. 2015, MNRAS, 452, 2127
Skilling, J. 2004, in American Institute of Physics Conference Series, 735, American Institute of Physics Conference Series, eds. R. Fischer, R. Preuss, & U. V. Toussaint, 395
Skilling, J. 2006, Bayesian Anal., 1, 833
Slumstrup, D., Grundahl, F., Silva Aguirre, V., & Brogaard, K. 2019, A&A, 622, A111
Smith, J. C., Stumpe, M. C., Van Cleve, J. E., et al. 2012, PASP, 124, 1000
Socrates, A., Katz, B., Dong, S., & Tremaine, S. 2012, ApJ, 750, 106
Sousa, S. G., Santos, N. C., Israelian, G., Mayor, M., & Udry, S. 2011, A&A, 533, A141
Speagle, J. S. 2020, MNRAS, 493, 3132
Spitoni, E., Recio-Blanco, A., de Laverny, P., et al. 2023, A&A, 670, A109
Stassun, K. G., Oelkers, R. J., Paegert, M., et al. 2019, AJ, 158, 138
Stevenson, A. T., Haswell, C. A., Faria, J. P., et al. 2025, MNRAS, 539, 727
Strakhov, I. A., Safonov, B. S., & Cheryasov, D. V. 2023, Astrophys, Bull., 78, 234
Stumpe, M. C., Smith, J. C., Van Cleve, J. E., et al. 2012, PASP, 124, 985
Stumpe, M. C., Smith, J. C., Catanzarite, J. H., et al. 2014, PASP, 126, 100
Telting, J. H., Avila, G., Buchhave, L., et al. 2014, Astron. Nachr., 335, 41
Tinetti, G., Drossart, P., Eccleston, P., et al. 2018, Exp. Astron., 46, 135
Tokovinin, A. 2018, PASP, 130, 035002
Tull, R. G., MacQueen, P. J., Sneden, C., & Lambert, D. L. 1995, PASP, 107, 251
Twicken, J. D., Clarke, B. D., Bryson, S. T., et al. 2010, SPIE Conf. Ser., 7740, 774023
Udry, S., Mayor, M., & Santos, N. C. 2003, A&A, 407, 369
Valenti, J. A., & Piskunov, N. 1996, A&AS, 118, 595
VanderPlas, J. T., & Ivezić, Ž. 2015, ApJ, 812, 18
VanderPlas, J., Connolly, A. J., Ivezic, Z., & Gray, A. 2012, in Proceedings of Conference on Intelligent Data Understanding (CIDU), 47
Vines, J. I., & Jenkins, J. S. 2022, MNRAS[arXiv:2204.03769]
Virtanen, P., Gommers, R., Oliphant, T. E., et al. 2020, Nat. Methods, 17, 261
von Zeipel, H. 1910, Astron. Nachr., 183, 345
Wang, X.-Y., Rice, M., Wang, S., et al. 2024, ApJ, 973, L21
Weiss, A., & Schlattl, H. 2008, Ap&SS, 316, 99
Winther, M. L., Aguirre Børsen-Koch, V., Rørsted, J. L., Stokholm, A., & Verma, K. 2023, MNRAS, 525, 1416
Wu, Y., & Murray, N. 2003, ApJ, 589, 605
Yee, S. W., Petigura, E. A., & von Braun, K. 2017, ApJ, 836, 77
Ziegler, C., Tokovinin, A., Briceño, C., et al. 2020, AJ, 159, 19

[1] astroCOALA, Department of Physics and Astronomy, Aarhus University, Ny Munkegade 120, 8000 Aarhus C, Denmark
[2] Dipartimento di Fisica, Università degli Studi di Torino, via Pietro Giuria 1, 10125, Torino, Italy
[3] McDonald Observatory and Center for Planetary Systems Habitability, The University of Texas, Austin, TX, USA
[4] Department of Physics and Astronomy, Chalmers University of Technology, Onsala Space Observatory, 439 92 Onsala, Sweden
[5] School of Physics & Astronomy, University of Birmingham, Edgbaston, Birmingham B15 2TT, UK
[6] Center for Astrophysics Harvard & Smithsonian, 60 Garden Street, Cambridge, MA 02138, USA
[7] Bozeman, MT 59718, USA
[8] SRON, Netherlands Institute for Space Research, Niels Bohrweg 4, 2333 CA, Leiden, The Netherlands
[9] Department of Physics and Astronomy, University College London, Gower Street, London WC1E 6BT, UK
[10] NASA Exoplanet Science Institute-Caltech/IPAC, Pasadena, CA 91125, USA
[11] Lowell Observatory, 1400 West Mars Hill Road, Flagstaff, AZ 86001, USA
[12] Department of Physics, Engineering and Astronomy, Stephen F. Austin State University, 1936 North St, Nacogdoches, TX 75962, USA
[13] Cerro Tololo Inter-American Observatory, Casilla 603, La Serena, Chile
[14] Department of Physics and Astronomy, The University of North Carolina at Chapel Hill, Chapel Hill, NC 27599-3255, USA
[15] NSF NOIRLab, 950 N. Cherry Ave., Tucson, AZ 85719, USA
[16] NASA Ames Research Center, Moffett Field, CA 94035, USA
[17] Sternberg Astronomical Institute Lomonosov Moscow State University, Universitetskii prospekt, 13, Moscow, Russia
[18] Instituto de Astrofísica de Canarias (IAC), 38205 La Laguna, Tenerife, Spain
[19] Departamento de Astrofísica, Universidad de La Laguna (ULL), E-38206 La Laguna, Tenerife, Spain
[20] Astrobiology Research Unit, Université de Liège, 19C Allée du 6 Août, 4000 Liège, Belgium
[21] Department of Earth, Atmospheric and Planetary Science, Massachusetts Institute of Technology, 77 Massachusetts Avenue, Cambridge, MA 02139, USA
[22] Acton Sky Portal private observatory, Acton, MA, USA
[23] SUPA Physics and Astronomy, University of St. Andrews, Fife KY16 9SS Scotland, UK
[24] South African Astronomical Observatory, PO Box 9, Observatory, Cape Town 7935, South Africa
[25] MIT Kavli Institute for Astrophysics & Space Research, Massachusetts Institute of Technology, Cambridge, MA 02139, USA
[26] AstroAI, Center for Astrophysics Harvard & Smithsonian, 60 Garden Street, Cambridge, MA 02138, USA

Appendix A: Additional tables

Table A.1. Space-based photometry.

Facility	Sectors/Date -/(UTC)	Cadence (min)	System
TESS	44, 45	10	TOI-5120
TESS	71, 72	2	TOI-5120
CHEOPS	2022-12-30	1	TOI-5120
CHEOPS	2024-02-02	1	TOI-5120
TESS	25	30	TOI-5699
TESS	51, 52	10	TOI-5699
TESS	78, 79	2	TOI-5699
TESS	26	30	TOI-2158
TESS	40, 53	2	TOI-2158

Table A.2. Radial velocities for TOI-5120, TOI-5699, and TOI-2158 (extract).

BJD (TDB)	RV (m s^{-1})	σ_{RV} (m s^{-1})	Instrument	TOI
2459620.713441	47758.90	16.30	TS23	5120
2459621.762558	47746.50	15.00	TS23	5120
⋮	⋮	⋮	⋮	⋮
2459622.444186	-1.90	8.00	FIES+	5120
2459623.447149	-22.60	7.60	FIES+	5120
⋮	⋮	⋮	⋮	⋮
2459978.991798	65128.50	15.50	TS23	5699
2459980.001616	65130.10	18.90	TS23	5699
⋮	⋮	⋮	⋮	⋮
2460779.707932	-30.90	9.50	FIES+	5699
2460800.562709	-25.30	9.10	FIES+	5699
⋮	⋮	⋮	⋮	⋮
2459302.926498	-64797.20	23.70	TS23	2158
2459308.917232	-64742.00	20.70	TS23	2158
⋮	⋮	⋮	⋮	⋮
2459425.453503	2.90	5.60	FIES+	2158
2459428.618606	144.70	14.10	FIES+	2158
⋮	⋮	⋮	⋮	⋮
2459332.677805	0.10	10.50	FIES	2158
2459339.681805	-37.90	8.70	FIES	2158
⋮	⋮	⋮	⋮	⋮

Notes. This table is available in its entirety at the CDS.

Table A.3. Varied parameters of the `Barbie`-MS grid with 5977 tracks.

Variable	Minimum	Maximum
M ($M_\odot$)	0.70	1.20
$[Fe/H]_{ini}$	−1.0	0.6
Y_{ini}	0.24	0.32
α_{MLT}	1.60	2.00

Notes. Evolution along the tracks is tracked from the zero-age main sequence until $\Delta\nu = 50\,\mu$Hz, and includes treatment of microscopic diffusion, but no convective overshoot.

Table A.4. Limb-darkening coefficients for the different band-passes for the observations of TOI-5120.

TOI-5120	$q_1 + q_2$	$q_1 - q_2$	q_1	q_2
TESS	0.62 ± 0.09	0.16	0.39 ± 0.04	0.23 ± 0.04
CHEOPS	0.68 ± 0.09	0.38	$0.53^{+0.05}_{-0.04}$	$0.15^{+0.05}_{-0.04}$
B	$0.83^{+0.08}_{-0.09}$	0.59	$0.71^{+0.04}_{-0.05}$	$0.12^{+0.04}_{-0.05}$
z-short	0.52 ± 0.09	0.12	$0.32^{+0.05}_{-0.04}$	$0.20^{+0.05}_{-0.04}$
i′	0.57 ± 0.09	0.19	0.38 ± 0.04	0.19 ± 0.04
r′	0.67 ± 0.09	0.29	$0.48^{+0.05}_{-0.04}$	$0.19^{+0.05}_{-0.04}$
TOI-5699	$q_1 + q_2$	$q_1 - q_2$	q_1	q_2
TESS	0.59 ± 0.07	−0.04	$0.28^{+0.03}_{-0.04}$	$0.32^{+0.03}_{-0.04}$
z-short	0.43 ± 0.07	0.10	0.26 ± 0.04	0.16 ± 0.04
TOI-2158	$q_1 + q_2$	$q_1 - q_2$	q_1	q_2
TESS	$0.60^{+0.06}_{-0.05}$	0.05	0.32 ± 0.03	0.28 ± 0.03
B	0.45 ± 0.09	0.15	0.30 ± 0.05	0.15 ± 0.05
z-short	0.98 ± 0.08	0.05	0.51 ± 0.04	0.46 ± 0.04
i′	$0.62^{+0.09}_{-0.08}$	0.74	0.68 ± 0.04	-0.06 ± 0.04

Notes. During the fit, we stepped in the sum of the limb darkening coefficients applying a gaussian prior with a width of 0.1, while fixing the difference.

Table A.5. Ground-based photometry.

Observatory	Aperture (m)	Location	Date (UTC)	Filter	Coverage	Planet
Acton Sky Portal	0.36	Acton, MA, USA	2023-04-09	*i*′	Ingress+80%	TOI-5120 b
Acton Sky Portal	0.36	Acton, MA, USA	2023-11-19	*r*′	Ingress+80%	TOI-5120 b
LCOGT-TFN	1.0	Tenerife, Canary Islands	2024-02-01	*B*	Ingress+50%	TOI-5120 b
LCOGT-TFN	1.0	Tenerife, Canary Islands	2024-02-01	*z*-short	Ingress+50%	TOI-5120 b
LCOGT-McD	1.0	McDonald Observatory, TX, USA	2024-02-02	*B*	Egress+90%	TOI-5120 b
LCOGT-McD	1.0	McDonald Observatory, TX, USA	2024-02-02	*z*-short	Egress+90%	TOI-5120 b
LCOGT-TFN	1.0	Tenerife, Canary Islands	2023-06-26	*z*-short	Full	TOI-5699 b
LCOGT-McD	0.4	McDonald Observatory, TX, USA	2020-08-06	Sloan *i*′	Full	TOI-2158 b
LCOGT-SAAO	1.0	Cape Town, South Africa	2021-06-05	*B*	Full	TOI-2158 b
LCOGT-SAAO	1.0	Cape Town, South Africa	2021-06-05	*z*-short	Full	TOI-2158 b

Table A.6. Spectroscopic parameters for TOI-5120, TOI-5699, and TOI-2158 modelled with SME compared to values from *Gaia* DR3 and EXOFOP.

Method	$T_{\rm eff}$ (K)	$\log g$ (cgs)	[Fe/H] (dex)	[Ca/H] (dex)	[Na/H] (dex)	$v \sin i_\star$ (km s^{-1})
			TOI-5120			
SME	5763 ± 90	4.18 ± 0.07	0.20 ± 0.07	0.25 ± 0.08	0.40 ± 0.09	4.8 ± 0.9
Gaia DR3	5823^{+12}_{-4}	4.12	···	···	···	···
EXOFOP[(a)]	5778 ± 103	4.12 ± 0.07	0.20 ± 0.01	···	···	···
			TOI-5699			
SME	5905 ± 100	4.05 ± 0.07	0.11 ± 0.05	0.20 ± 0.06	0.25 ± 0.05	4.3 ± 1.2
Gaia DR3	5818 ± 3	4.11	···	···	···	···
EXOFOP[(b)]	5900 ± 143	3.99 ± 0.08	0.02 ± 0.01	···	···	···
			TOI-2158			
SME	5399 ± 64	4.00 ± 0.05	0.19 ± 0.09	0.19 ± 0.11	0.42 ± 0.12	3.6 ± 1.0
Gaia DR3	$5400 \pm^{+10}_{-24}$	4.23	···	···	···	···
EXOFOP[(c)]	5389 ± 123	4.06 ± 0.08	0.39	···	···	···
SPC	5673 ± 50	4.19 ± 0.05	0.47 ± 0.08	···	···	3.7 ± 0.5

[(a)] https://exofop.ipac.caltech.edu/tess/target.php?id=58723861
[(b)] https://exofop.ipac.caltech.edu/tess/target.php?id=224328450
[(c)] https://exofop.ipac.caltech.edu/tess/target.php?id=342642208

Table A.7. Comparison of stellar parameters of TOI-2158, TOI-5120, and TOI-5699 modelled using the spectroscopic values from the SME analysis.

Method	$M_\star$ ($M_\odot$)	$R_\star$ ($R_\odot$)	$\rho_\star$ (g cm^{-3})	$L_\star$ ($L_\odot$)	Age (Gyr)
			TOI-5120		
ARIADNE	1.154 ± 0.053	1.413 ± 0.035	0.58 ± 0.05	2.04 ± 0.10	5.7 ± 0.8
BASTA	1.12 ± 0.05	1.42 ± 0.05	0.55 ± 0.07	1.98 ± 0.09	7.5 ± 1.5
			TOI-5699		
ARIADNE	1.158 ± 0.065	1.676 ± 0.051	0.35 ± 0.04	3.10 ± 0.10	$6.0^{+0.5}_{-3.5}$
BASTA	1.13 ± 0.04	1.64 ± 0.06	0.36 ± 0.04	2.87 ± 0.14	6.6 ± 0.7
			TOI-2158		
ARIADNE	0.984 ± 0.032	1.453 ± 0.017	0.35 ± 0.04	1.59 ± 0.05	$13.1^{+0.4}_{-1.5}$
BASTA	0.975 ± 0.019	1.50 ± 0.05	0.40 ± 0.04	1.68 ± 0.08	14.0 ± 0.9
BASTA [(a)]	1.12 ± 0.05	1.32 ± 0.04	0.69 ± 0.06	1.57 ± 0.06	7.7 ± 1.6

Notes. [(a)] Spectroscopic values from SPC.

Table A.8. Posterior values from the joint fit of the RVs and TESS photometry for TOI-5120 and TOI-5699 assuming a circular orbit.

	TOI-5120	TOI-5699
	Planet b	
T_0 (BJD_{TDB})	2460267.9302(3)	2459704.1558(8)
P (d)	24.91645(2)	22.01850(4)
$a/R_\star$	$28.2^{+0.8}_{-0.7}$	$28.5^{+1.9}_{-2.4}$
$\cos i$	0.012 ± 0.003	0.029 ± 0.003
$R_p/R_\star$	0.0703 ± 0.0005	$0.0625^{+0.0012}_{-0.0011}$
K (m s^{-1})	77 ± 2	$15.5^{+1.6}_{-1.7}$
	System/instrument	
γ_1 (m s^{-1})	47781 ± 3	65122.9 ± 1.3
γ_2 (m s^{-1})	$38.7^{+2.0}_{-1.8}$	-45 ± 3
σ_1 (m s^{-1})	17^{+2}_{-3}	$0.009^{+0.059}_{-0.009}$
σ_2 (m s^{-1})	$0.19^{+3.11}_{-0.19}$	$0.006^{+0.027}_{-0.006}$

Notes. Symbols have the same meaning as in Table 4.

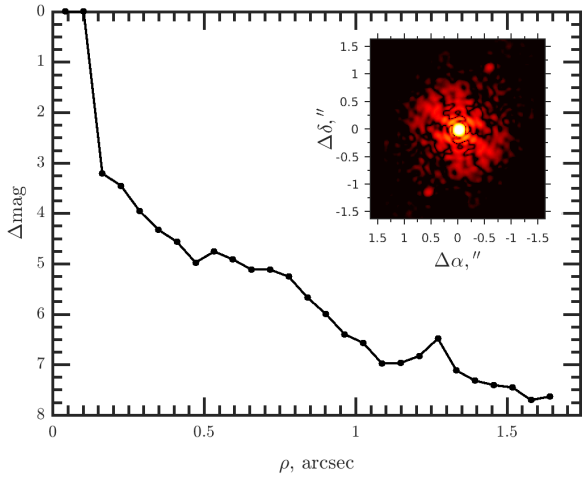


Fig. B.2. SAI-2.5m speckle sensitivity curve and ACF of TOI-5120 in the I band.

Appendix B: Additional figures

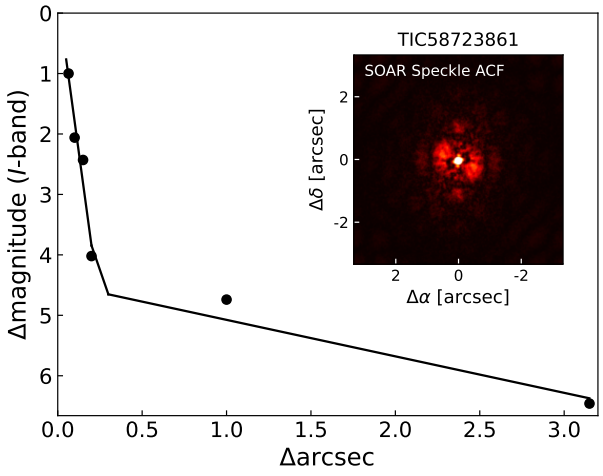


Fig. B.1. SOAR 5σ detection sensitivity and speckle auto-correlation function imaging for the TOI-5120 system.

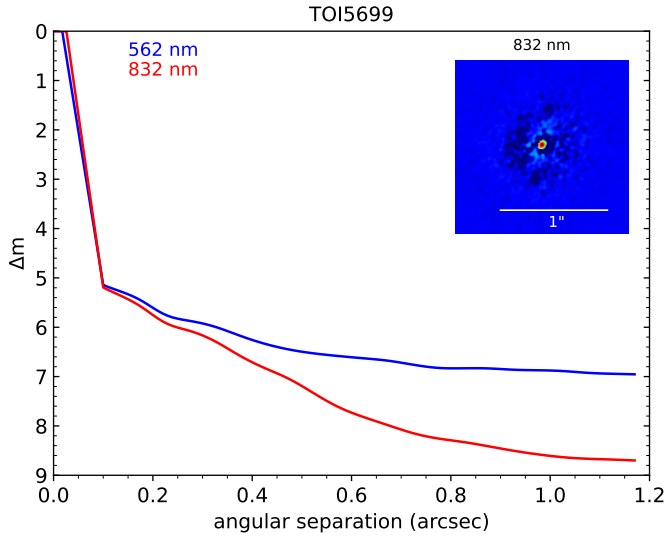


Fig. B.3. Gemini North speckle optical 5σ contrast curves and the 832 nm reconstructed image for the TOI 5699 system.

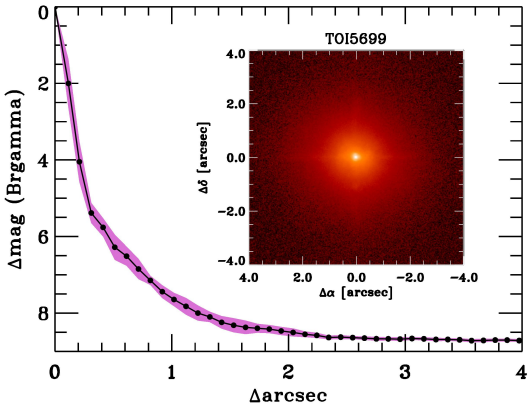


Fig. B.4. Palomar NIR AO close-in view and sensitivity curve for the TOI-5699 system.

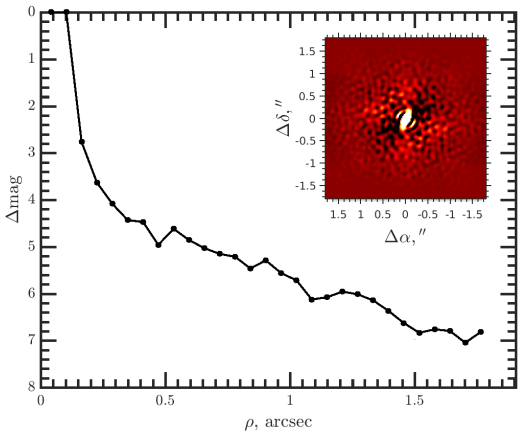


Fig. B.5. SAI-2.5m speckle sensitivity curve and ACF of TOI-5699 in the *I* band.

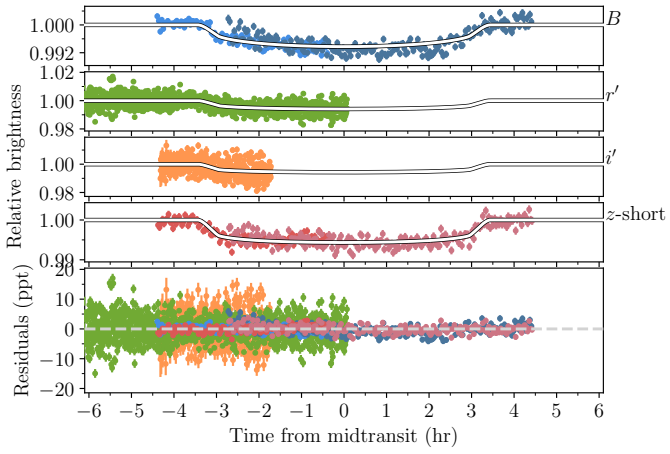


Fig. B.6. Ground-based follow-up photometry for TOI-5120 b. Observations were carried out in the *B* (blue), *r*′ (green), *i*′ (orange), and *z*-short (red) band-passes. The best-fitting transit model for TOI-5120 b for each bandpass is overplotted. For *B* and *z*-short there are two sets of observations (see Fig. B.11).

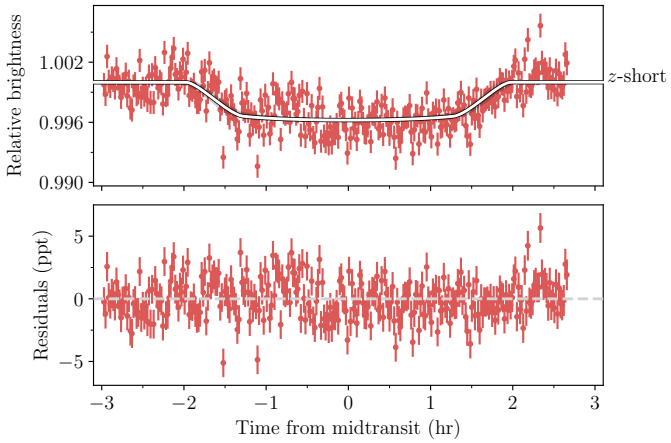


Fig. B.7. Ground-based follow-up photometry for TOI-5699 b carried out using the *z*-short (red) band-pass. The best-fitting transit model for TOI-5699 b is overplotted.

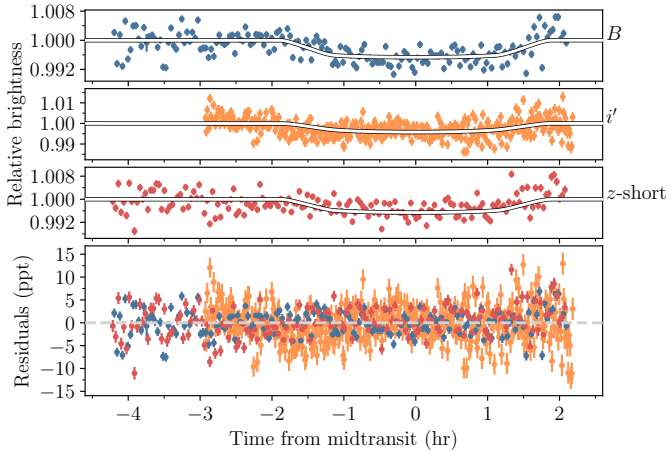


Fig. B.8. Ground-based follow-up photometry for TOI-2158 b. Observations were carried out in the *B* (blue), *i*′ (orange), and *z*-short (red) band-passes. The best-fitting transit model for TOI-2158 b for each band-pass is overplotted.

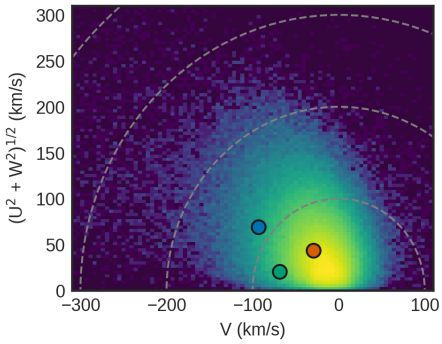


Fig. B.9. Plot of the Galactic orbital motions of the three stars, compared single stars from *Gaia* DR3 with reliable astrometric data and available line-of-sight velocities (`astrometric_params_solved = 95`, `rv_nb_transits > 0`, `ruwe < 1.4`, and `non_single_star = 0`). The Toomre diagram shows the positions of our host stars in heliocentric Cartesian velocity space, demonstrating that they are members of the Galactic disk. TOI-5120, TOI-5699, and TOI-2158 are shown with green, orange, and blue markers, respectively.

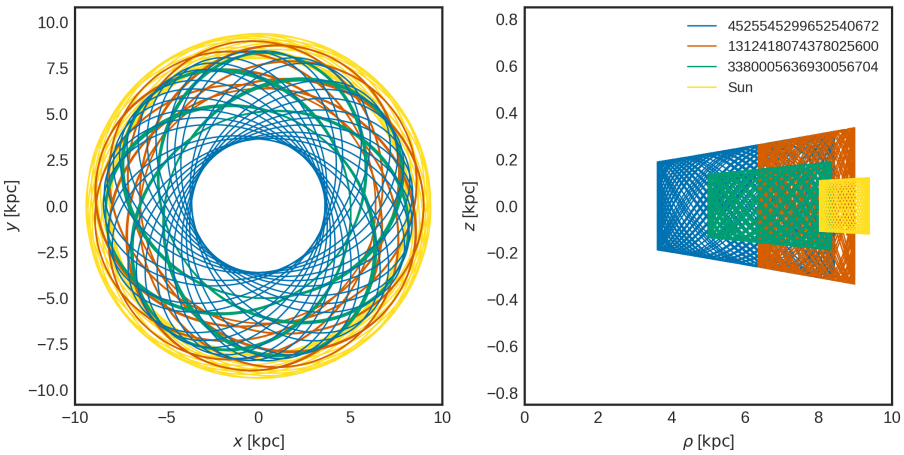


Fig. B.10. Galactic orbits of the three host stars around the Milky Way's centre. The orbit of the Sun is shown for comparison. Colour-coding is the same as in Fig. B.9.

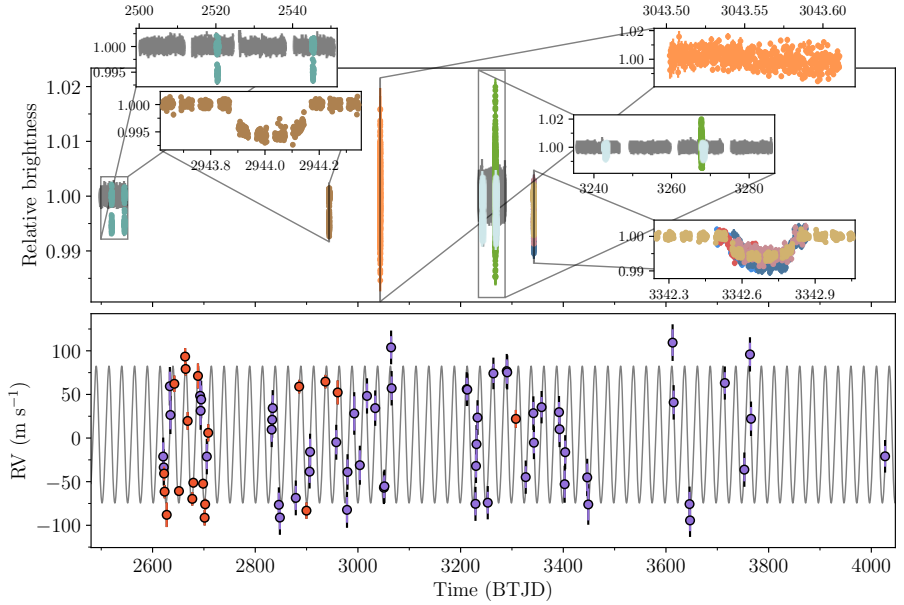


Fig. B.11. Time series of TOI-5120. *Top:* TESS photometry shown in gray with points around transits marked with green colors as shown in Fig. 1 (10-min cadence in dark and 2-min cadence in light). The CHEOPS observations are shown as brown and tan markers. Ground-based . *Bottom:* RVs obtained with TS23 (purple) and FIES (orange) overplotted on the best-fitting orbital solution.

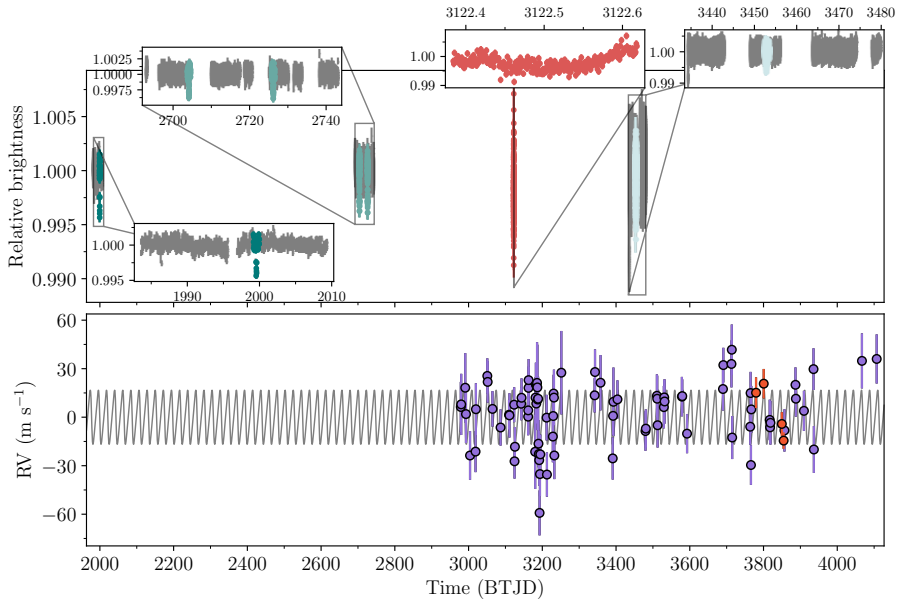


Fig. B.12. Time series of TOI-5699. *Top:* TESS photometry shown in gray with markers around transits colored as in Fig. 3 (30-min cadence in dark green, 10-min cadence in lighter green, and 2-min in pale blue). The single ground-based transit taken with the *z*-short filter from LCOGT is shown in red. *Bottom:* RVs obtained with TS23 overplotted on the best-fitting orbital solution.

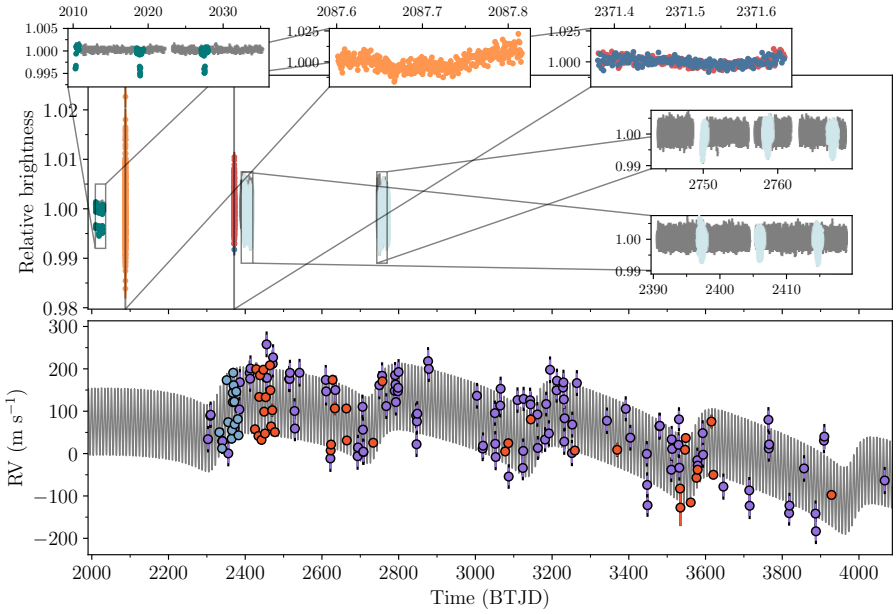


Fig. B.13. Time series of TOI-2158. *Top:* TESS photometry shown in gray with points around transits marked with green colors as shown in Fig. 4 (30-min cadence in dark and 2-min cadence in light). Ground-based photometry from LCOGT are shown as red (i'), blue (B), and orange (z-short) markers. The insets show the raw, continuous photometric time series. *Bottom:* RVs obtained with TS23 (purple), FIES (light blue), and FIES+ (orange) overplotted on the best-fitting orbital solution as Figs. 8 and 9. The white line denotes the long-term trend.

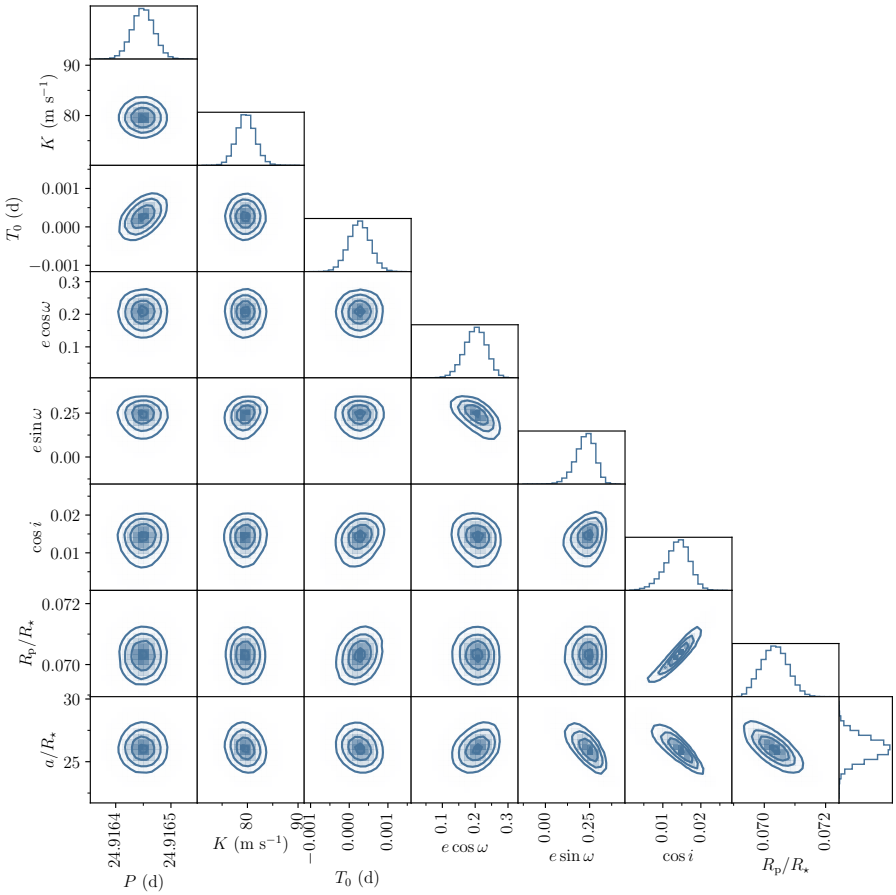


Fig. B.14. Correlation plot of the key stepping parameters of the MCMC carried out for TOI-5120. T_0 is offset by 2460267.93.

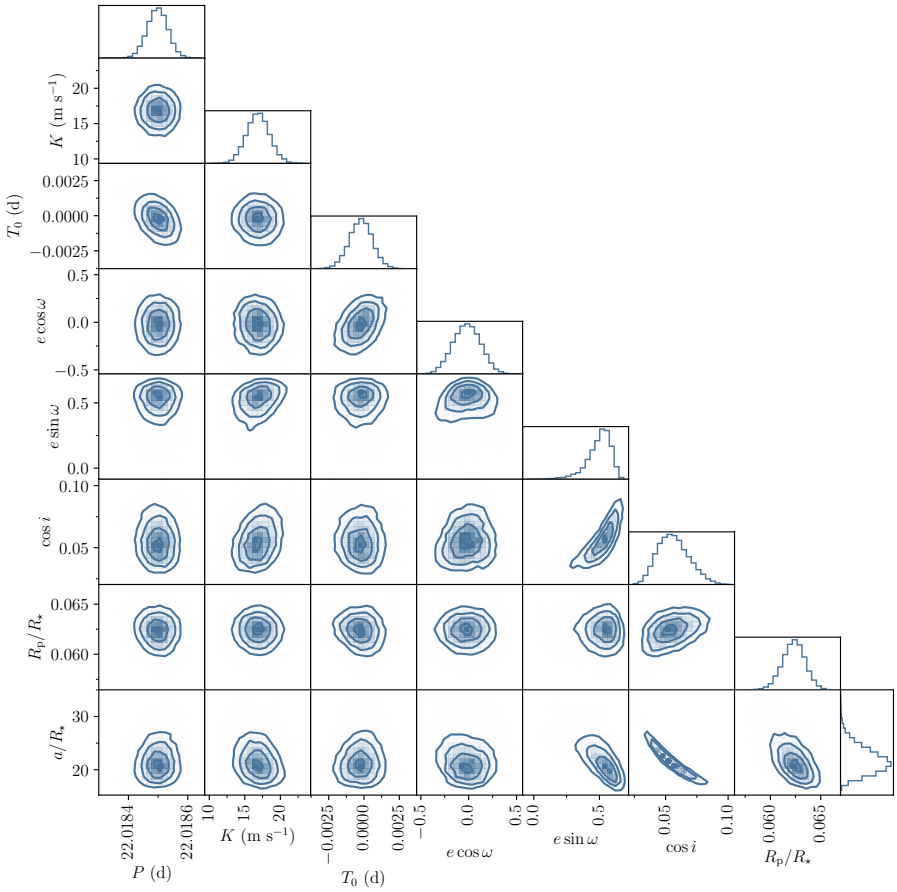


Fig. B.15. Correlation plot of the key stepping parameters of the MCMC carried out for TOI-5699. T_0 is offset by 2459704.156.

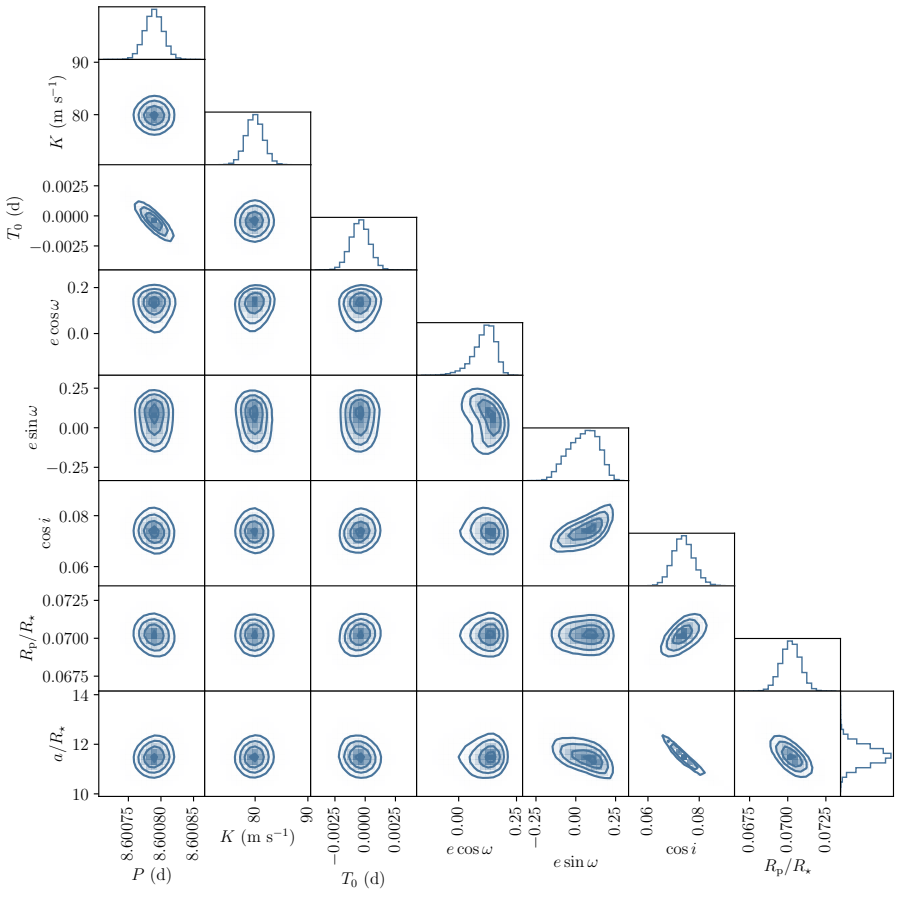


Fig. B.16. Correlation plot of the key stepping parameters of the MCMC carried out for TOI-2158 b. T_0 is offset by 2459018.92.

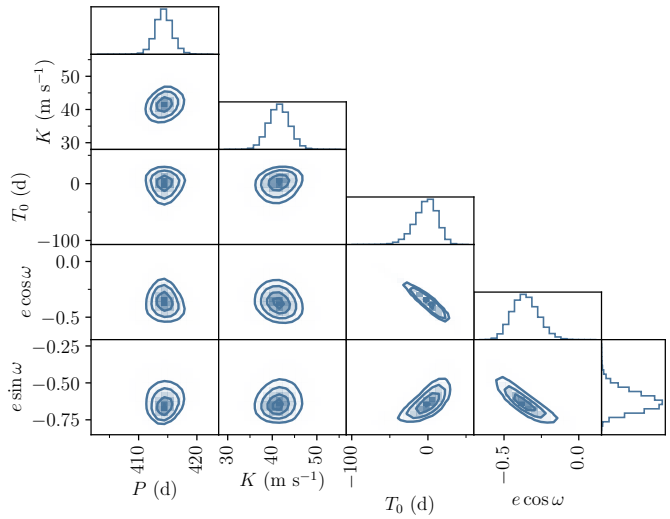


Fig. B.17. Correlation plot of the key stepping parameters of the MCMC carried out for TOI-2158 c. T_0 is offset by 2459620.

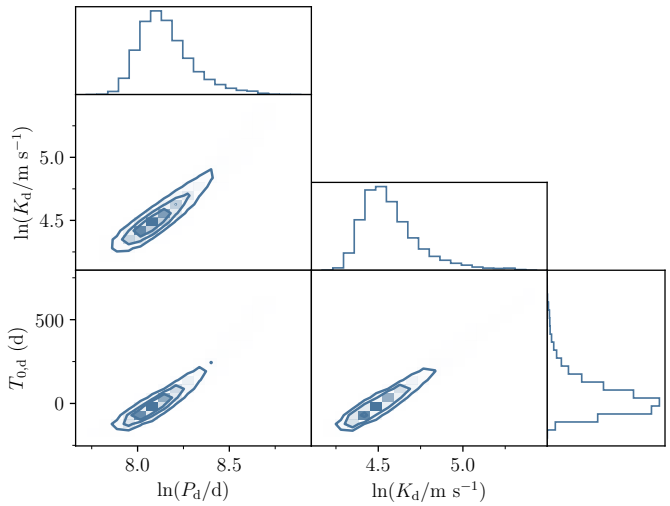


Fig. B.18. Correlation plot of the key stepping parameters of the MCMC carried out for TOI-2158 d. T_0 is offset by 2460506.